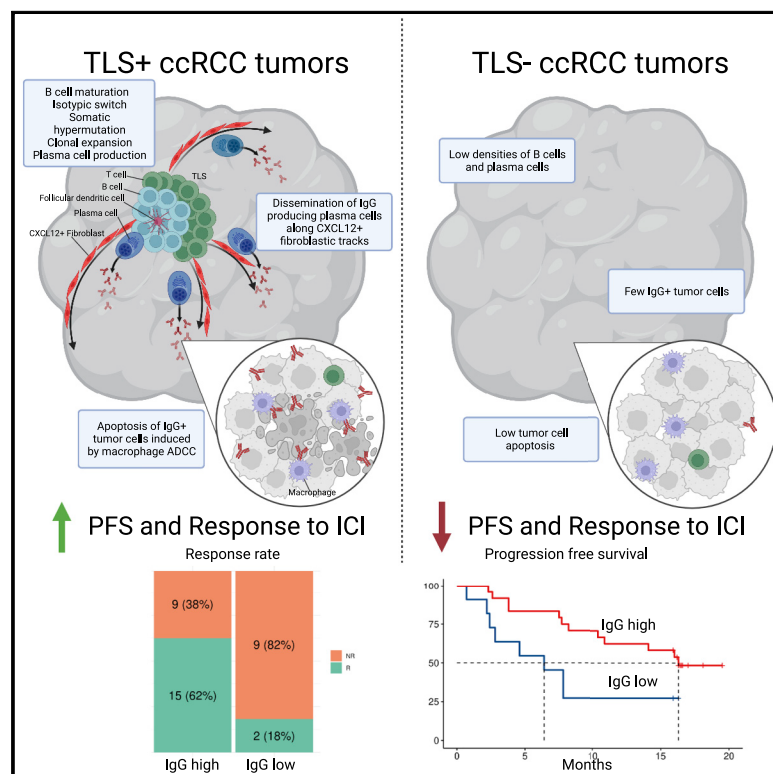


# Immunity

## Tertiary lymphoid structures generate and propagate anti-tumor antibody-producing plasma cells in renal cell cancer

### Graphical abstract



### Authors

Maxime Meylan, Florent Petitprez,  
Etienne Becht, ..., Aurélien de Reyniès,  
Catherine Sautès-Fridman,  
Wolf Herman Fridman

### Correspondence

herve.fridman@crc.jussieu.fr

### In brief

Meylan et al. show that tertiary lymphoid structures found in tumors are sites of generation of fully mature B cell immunity. Plasma cells disseminate into tumor beds, producing antibodies that bind to tumor cells and initiate their apoptosis, providing a mechanism to support cancer immunotherapies that modulate the tumor microenvironment.

### Highlights

- Tertiary lymphoid structures are sites of *in situ* B cell maturation toward plasma cells
- IgG+ and IgA+ plasma cells disseminate into the tumor tissue along fibroblastic tracks
- Tumor cells are labeled by locally produced IgG
- Patients with IgG-labeled tumor cells have high response rate to ICI and prolonged PFS



## Article

# Tertiary lymphoid structures generate and propagate anti-tumor antibody-producing plasma cells in renal cell cancer

Maxime Meylan,<sup>1</sup> Florent Petitprez,<sup>2,3</sup> Etienne Becht,<sup>2</sup> Antoine Bougoün,<sup>1</sup> Guilhem Pupier,<sup>1</sup> Anne Calvez,<sup>1</sup> Ilenia Giglioli,<sup>1</sup> Virginie Verkarre,<sup>4,11,12</sup> Guillaume Lacroix,<sup>1</sup> Johanna Verneau,<sup>1</sup> Chen-Ming Sun,<sup>1</sup> Pierre Laurent-Puig,<sup>5</sup> Yann-Alexandre Vano,<sup>1,2,3,6,11,12</sup> Reza Elaïdi,<sup>7</sup> Arnaud Méjean,<sup>8</sup> Rafaël Sanchez-Salas,<sup>9</sup> Eric Barret,<sup>9</sup> Xavier Cathelineau,<sup>9</sup> Stephane Oudard,<sup>6,11</sup> Claude-Agnès Reynaud,<sup>10</sup> Aurélien de Reyniès,<sup>2,3,5,11,13,14</sup> Catherine Sautès-Fridman,<sup>1,13,14</sup> and Wolf Herman Fridman<sup>1,13,14,15,\*</sup>

<sup>1</sup>Centre de Recherche des Cordeliers, Sorbonne Université, INSERM, Université de Paris, Equipe labellisée Ligue Contre le Cancer, 75006 Paris, France

<sup>2</sup>Programme Cartes d'Identité des Tumeurs (CIT), Ligue Nationale Contre Le Cancer, 75013 Paris, France

<sup>3</sup>MRC Centre for Reproductive Health, Queen's Medical Research Institute, The University of Edinburgh, Edinburgh EH16 4TJ, UK

<sup>4</sup>Département de pathologie, Hôpital européen Georges Pompidou, Assistance Publique-Hôpitaux de Paris - Paris Centre, 75015 Paris, France

<sup>5</sup>Centre de Recherche des Cordeliers, Sorbonne Université, INSERM, Université de Paris, EPIGENETEC, 75006 Paris, France

<sup>6</sup>Département d'oncologie médicale, Hôpital européen Georges Pompidou, Assistance Publique-Hôpitaux de Paris - Paris Centre, F-75015 Paris, France

<sup>7</sup>Association pour la Recherche de Thérapeutiques Innovantes en Cancérologie, 75015 Paris, France

<sup>8</sup>Département d'urologie, Hôpital européen Georges Pompidou, Université de Paris, 75015 Paris, France

<sup>9</sup>Département d'urologie, Institut Mutualiste Montsouris, Université de Paris, 75014 Paris, France

<sup>10</sup>Institut Necker Enfants Malades (INEM), INSERM U1151/CNRS UMRS8253, Université de Paris, 75015 Paris, France

<sup>11</sup>Université de Paris, 75006 Paris, France

<sup>12</sup>PARCC, INSERM, Equipe Labellisée Ligue contre le Cancer, 75015 Paris, France

<sup>13</sup>These authors contributed equally

<sup>14</sup>Senior author

<sup>15</sup>Lead contact

\*Correspondence: [herve.fridman@crc.jussieu.fr](mailto:herve.fridman@crc.jussieu.fr)

<https://doi.org/10.1016/j.immuni.2022.02.001>

## SUMMARY

The presence of intratumoral tertiary lymphoid structures (TLS) is associated with positive clinical outcomes and responses to immunotherapy in cancer. Here, we used spatial transcriptomics to examine the nature of B cell responses within TLS in renal cell carcinoma (RCC). B cells were enriched in TLS, and therein, we could identify all B cell maturation stages toward plasma cell (PC) formation. B cell repertoire analysis revealed clonal diversification, selection, expansion in TLS, and the presence of fully mature clonotypes at distance. In TLS+ tumors, IgG- and IgA-producing PCs disseminated into the tumor beds along fibroblastic tracks. TLS+ tumors exhibited high frequencies of IgG-producing PCs and IgG-stained and apoptotic malignant cells, suggestive of anti-tumor effector activity. Therapeutic responses and progression-free survival correlated with IgG-stained tumor cells in RCC patients treated with immune checkpoint inhibitors. Thus, intratumoral TLS sustains B cell maturation and antibody production that is associated with response to immunotherapy, potentially via direct anti-tumor effects.

## INTRODUCTION

Tertiary lymphoid structures (TLS) are found in tissues subjected to chronic inflammation and antigen persistence in autoimmune diseases, chronic infections, graft rejection, and cancers (Dieu-Nosjean et al., 2014; Pitzalis et al., 2014). The presence and density of intra-tumoral TLS correlate with favorable prognosis in many cancer types (Sautès-Fridman et al., 2019).

TLS are organized lymphoid aggregates formed on a network of fibroblasts and comprising a T cell zone, in which mature dendritic cells are in contact with T cells, and a follicular B cell zone (Sautès-Fridman et al., 2019). Mature TLS are defined by the presence of a germinal center (GC) containing T follicular helper (Tfh) cells and follicular dendritic cells in close contact with B cells (Germain et al., 2014; Gu-Trantien et al., 2013). Recent evidence supports the proposition that GC-containing mature TLS, rather than early TLS without a GC, are associated with clinical



benefits in hepatocellular carcinoma (Calderaro et al., 2018; Meylan et al., 2020), lung squamous cell carcinoma (Siliqi et al., 2018), colorectal cancer (Posch et al., 2018), and pancreatic cancer (Gunderson et al., 2021). The main function of the GC is to produce memory B cells and long-lived plasma cells (PCs) secreting high-affinity antibodies (Bannard and Cyster, 2017; Kuroski et al., 2015; MacLennan, 1994). High expression levels of B cell and PC transcriptomic signatures and high PC densities correlate with longer survival in several cancer types (Fridman et al., 2021). The presence of B cells and mature TLS predict therapeutic responses to immune checkpoint inhibitors (ICI) and survival, more accurately than T cells, in soft tissue sarcoma (Petitprez et al., 2020; Vanhersecke et al., 2021), melanoma (Cabrita et al., 2020; Helmink et al., 2020), renal cell cancer (Helmink et al., 2020; Vanhersecke, 2021), non-small cell lung cancer (Vanhersecke, 2021), urothelial cancer (Gao et al., 2020; Vanhersecke, 2021), and other cancer types (Vanhersecke, 2021). The mechanisms by which B cells and PCs influence clinical outcome and response to ICI are unknown (Fridman et al., 2021). Although some reports showed that intra-tumoral B cells can produce IgG (Garaud et al., 2019) and IgA (Shalapour et al., 2017) antibodies directed toward tumor-associated antigens in some cancers (Biswas et al., 2021; Germain et al., 2014; Katoh et al., 2017; Moftfort et al., 2017; Nielsen et al., 2012; Wieland et al., 2021), there is no proof that they originate from B cell differentiation taking place inside tumors, particularly at the TLS site.

In the present work, we addressed the question of the role of TLS as drivers of *in situ* maturation of B cells, generation of antibody-producing PCs, and their impact on the response to ICI. We report the spatially resolved transcriptomic architecture of the tumor microenvironment (TME) of clear cell renal cell carcinoma (ccRCC) primary tumors. By focusing on TLS and their vicinity, we show the presence of B cells at different maturation stages, supporting the generation of a B cell response. We evidence somatic hypermutation, clonal selection, and expansion of B cells, as well as immunoglobulin production by PC, demonstrating that a full B cell response is generated inside tumors. In addition, we find intra-tumoral dissemination of IgG- and IgA-positive PCs along CXCL12-positive fibroblastic tracks. We show that antibodies, mostly IgG, are bound to tumor cells, and their presence is associated with caspase-dependent tumor cell apoptosis. The detection of macrophages in close vicinity to IgG-stained tumor cells presenting caspase 3 activation suggests that they may be effectors by inducing IgG-mediated tumor cell death. Finally, patients with high numbers of IgG-positive tumor cells exhibit a high response rate and longer PFS in response to ICI.

## RESULTS

Primary tumors ( $n=130$ ) from three cohorts of treatment-naïve patients with ccRCC were analyzed (Table S1), 46 from the prospective translational research program ExhauCRF conducted at Hôpital Européen Georges Pompidou (HEGP), 25 from the Institut Mutualiste Montsouris (IMM), and 59 from the French multi-center BIOMarker Driven Trial With Nivolumab and Ipilimumab or VEGFR tKi in Naïve Metastatic Kidney Cancer (BIONIKK) clinical trial, which included 199 metastatic patients treated either with Nivolumab (N), Nivolumab + Ipilimumab (NI) or tyrosine kinase VEGFR inhibitors (TKI) (Vano et al., 2020). The components and

architecture of the TME were characterized by spatial transcriptomics on 24 tumors and spatial imaging on a total of 130 tumors using immunohistochemistry (IHC), multiplex immunofluorescence (IF) techniques, and an artificial intelligence (AI) based proximity assessment method (Figure S1; Table S1; STAR Methods).

### Spatial TME architecture unveils areas of B cell rich hot spots in TLS+ tumors

To analyze the impact of TLS on the TME architecture, we used the Visium spatial transcriptomics technology from 10X Genomics. It measures the full transcriptome at a spatial resolution using spatially barcoded oligonucleotides located in spots with a 55  $\mu\text{m}$  diameter. This allows to quantify the spatial gene expression in up to 5,000 spots.

Spatial transcriptomics was performed on 24 ccRCC primary tumors using frozen ( $n=12$ ) and FFPE sections ( $n=12$ ) (Table S1). The overall organization of each tumor and presence and localization of TLS were annotated by a trained pathologist (VV) after H&E staining of the sections (Figure 1A; Data S1). Figure 1 illustrates one TLS+ frozen tumor (Figures 1A–1C), one TLS+ FFPE tumor (Figures 1D–1F), and one TLS– frozen tumor (Figures 1G–1I). Expression of carbonic anhydrase 9 (protein name: CAIX, gene name: Ca9), a marker of ccRCC tumor cells, was detected in 23/24 tumors in accordance with its expression in most ccRCC tumors (Courcier et al., 2020) and was found evenly distributed in tumor sections (Figures 1B, 1E, and 1H; Data S1). Distribution of immune and stromal cell populations of the TME was evaluated with microenvironment cell populations (MCP)-counter which estimates cell type abundance from transcriptomic profiles (Becht et al., 2016a). In the TLS+ tumors illustrated in Figure 1, the B lineage (which contains genes identifying all the maturation steps from naive cells to PCs) and T cell (which identifies the different T cell populations) gene signatures were preferentially expressed in hot spots located within the TLS areas (Figures 1C and 1F; Data S1). Figure S2 illustrates, in one frozen (Figure S2A) and one FFPE (Figure S2B) tumor, that TLS areas had higher distribution of the B lineage and T cell scores compared with the rest of the tumor tissue ( $p < 2e-16$  respectively). These tumors exhibited low expression of the CD8 T cell signature, with slight enrichment in the TLS areas ( $p = 0.017$ , Figure S2A). Monocytic lineage signature was slightly higher in TLS ( $p = 0.00081$  and  $p = 0.035$ , Figures S2A and S3B, respectively), while NK cells were more diffusely distributed throughout the tumor section ( $p = 0.67$ , Figure S2A;  $p = 0.018$ , Figure S2B). Endothelial cells and neutrophils were evenly distributed with lower scores inside TLS ( $p = 3e-04$  and  $p = 0.048$ , respectively, Figure S2A;  $p = 2.5e-11$  and  $p = 0.6$ , respectively, Figure S2B), whereas high expression of the fibroblastic signature was found in the TLS areas (Figures 1C, 1F, and S2A,  $p < 2e-16$ , Figure S2B,  $p = 0.0039$ ). The TLS– tumor did not show such organized pattern, with MCP-counter analysis revealing very low and diffusely distributed B lineage scores, as well as dispersed localization of other immune and stromal signatures (Figure 1I; Data S1). These different patterns of TME spatial organization were consistently identifiable in the 8 TLS+ and 4 TLS– frozen tumors as well as in 10 TLS+ and 2 TLS– FFPE tumors (Data S1), suggesting an association of TLS with expression of B lineage, T cells, and fibroblasts signatures.

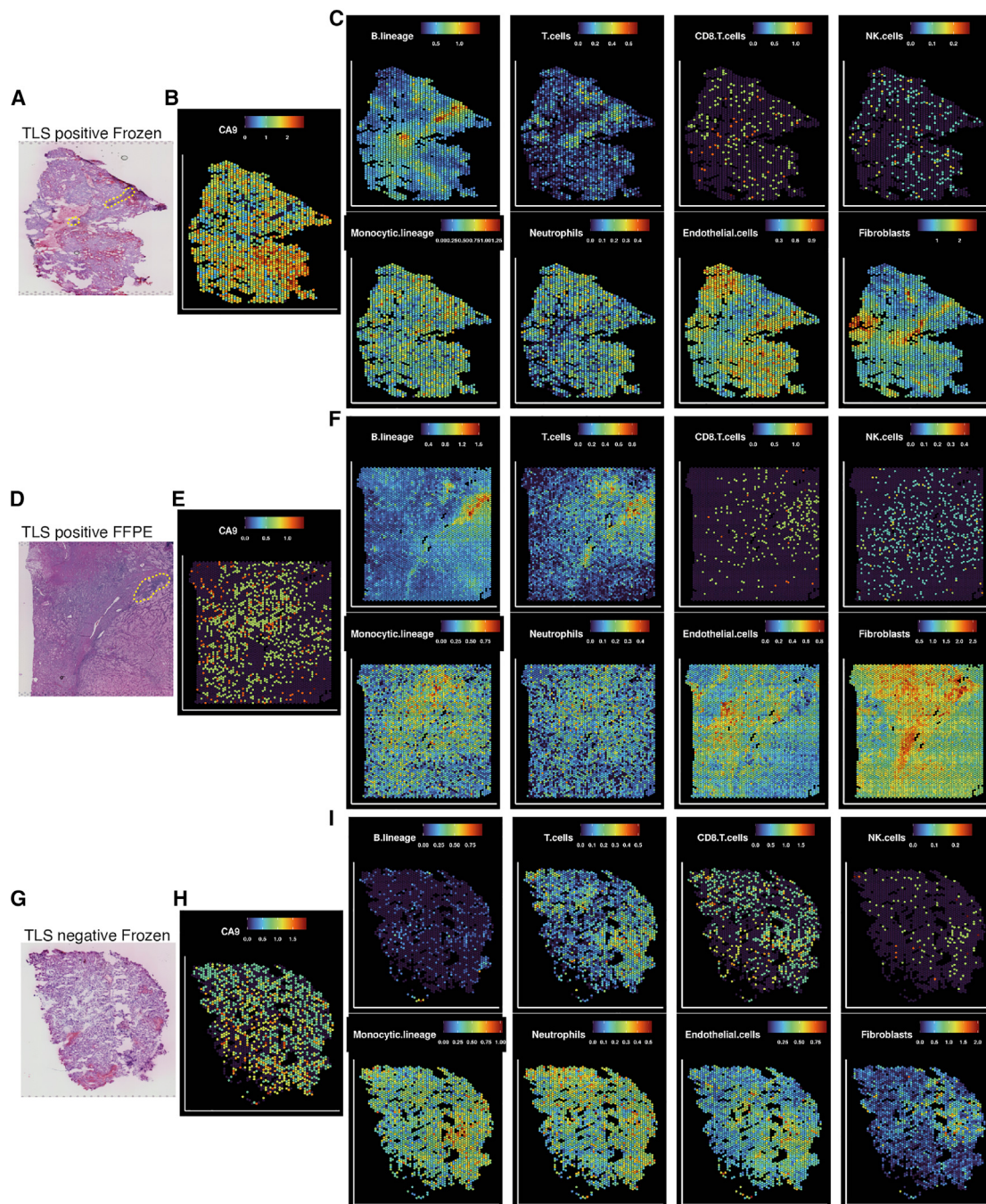


**Figure 1. Spatial transcriptomics of immune and stromal cell populations in the tumor microenvironment**

(A–F) Panels illustrate a frozen and an FFPE tumor with TLSs, respectively.

(G–I) Panels present a frozen tumor with no TLS.

(A, D, and G) Pathologist's annotations of the TLS areas on H&E slides used for the spatial transcriptomics assay, yellow = TLS areas.

(B, E, and H) Expression of the tumoral ccRCC marker CA9. (C, F, and I) Abundance estimation of 8 immune and stromal cell populations by MCP-counter.

#### Immunoglobulin (Ig) gene expression inside and at distance from TLS

To determine the transcriptomic imprint of TLS in tumors, we performed differential gene expression analysis between TLS and tumor areas, after having confirmed the H&E-defined TLS

location (Figures 2A and 2F) by triple IF labeling (CD20/CD3/PD-1) on a consecutive slide for frozen sections (Figure 2B; Data S2) and CD3/CD20 labeling by IHC for FFPE samples (Figure 2G; Data S2). Discovery of the TLS imprint signature was performed on 4 frozen TLS+ tumors by leave-one-out cross

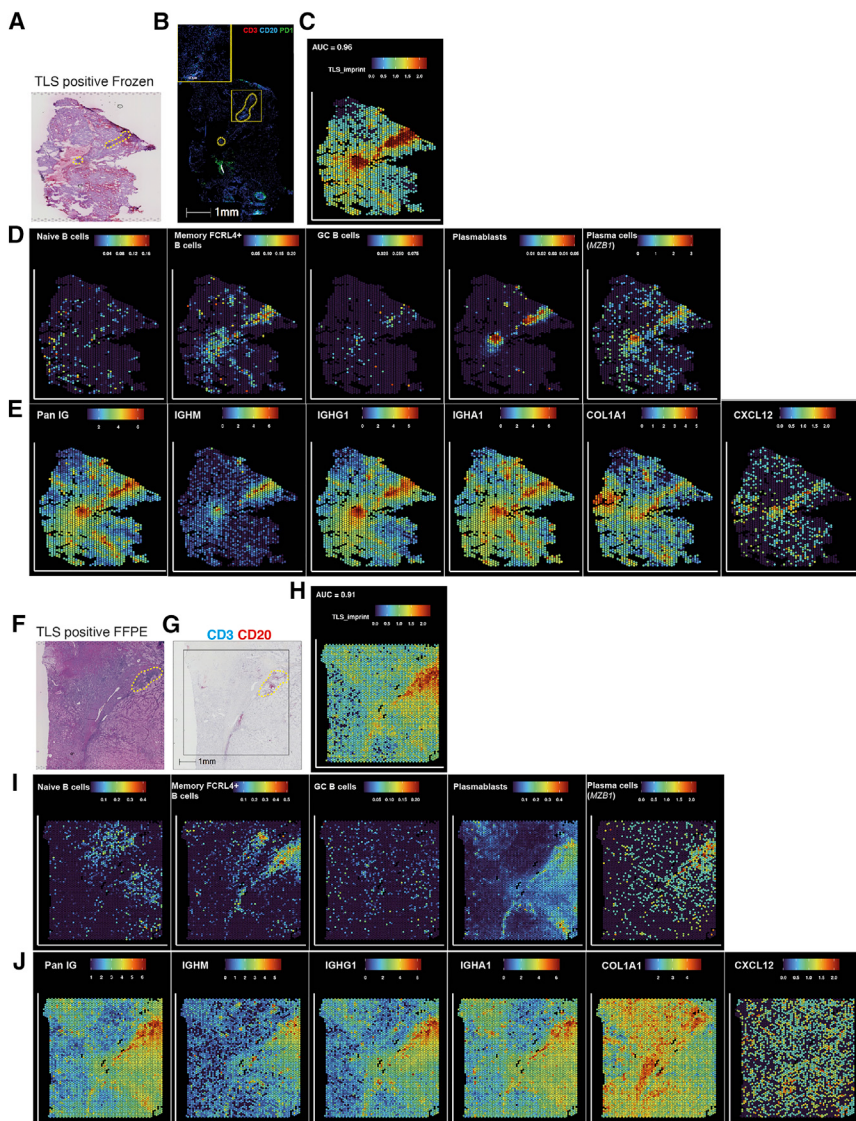


**Figure 2. Spatial co-localization of TLS with gene signatures of B cell subtypes, plasma cells, immunoglobulins, and fibroblasts**

(A and F) H&E image of a frozen and an FFPE TLS+ tumor used for the spatial transcriptomic assay, yellow lines delineate pathologically identified TLS areas.

(B and G) TLS confirmation by immunofluorescence on the consecutive slides of the frozen tumor (red = CD3, blue = CD20, green = PD1). Zoom on the TLS vicinity on the top left highlighted by a yellow square (B); or by IHC on a section from the same block of the FFPE tumor (blue = CD3, red = CD20). (G) The dark square indicates the area corresponding to the spatial transcriptomic assay. (C and H) Expression of the TLS imprint signature. (D and I) Mapping of B cell subsets defined in single cell analyses and expression of *MZB1* gene identifying PCs.

(E and J) Average expression of the pan Ig genes *IGKC* and *JCHAIN*, gene expression of the non-switched *IGHM* gene, the switched immunoglobulin genes *IGHG1* and *IGHG4*, and the fibroblast markers *COL1A1* and *CXCL12*.

validation, a method that performs sequential permutations by identifying genes from 3 tumors and validating them on the fourth one. Genes with an average fold change over 2 and adjusted p value under 0.05 (Bonferroni correction) were considered for the analysis (Figure S3A). We selected in the signature the genes that individually reached an area under the curve (AUC) of 0.7 in at least 3 TLS+ tumors (Figures S3B and S3C), which led to a 29 gene TLS imprint signature. This signature included 12 immunoglobulin genes (*IGHA1*, *IGHG1*, *IGHG2*, *IGHG3*, *IGHG4*, *IGHGP*, *IGHM*, *IGKC*, *IGLC1*, *IGLC2*, *IGLC3*, and *JCHAIN*), 5 B cells markers (*CD79A*, *FCRL5*, *MZB1*, *SSR4*, and *XBP1*), 2 T cells markers (*TRBC2* and *IL7R*), 2 fibroblasts markers (*CXCL12*, *LUM*), 2 complement protein coding genes (*C1QA* and *C7*), and *CD52*, *APOE*, *PTLP*, *PTGDS*, *PIM2*, and *DERL3* genes. This 29 genes signature, which is a marker of TLS imprint, featured AUC ranging from 0.89 to 0.97 in discovery frozen TLS+ tumors and from 0.77 to 0.94 in the validation on the remaining frozen TLS+ tumors (Figures 2A–2C; Data S2) (one tumor with an AUC of 0.55 was of poor RNA quality and had lobular

tumor tissue organization Data S2, tumor id c\_5). This signature was further validated on the 12 FFPE tumors (Figures 2F–2H; Data S2) with AUC ranging from 0.75 to 0.93 in the 9/10 TLS+ tumors, with the exception of one sample (c\_20) which had an AUC of 0.62 and a weak expression of the TLS imprint signature. This tumor was found to lack markers of TLS maturity, such as *CD23* and *BCL6*, and peripheral node addressin-positive (PNAd+) high endothelial venules (HEVs) (Figure 5A). Only sparse expression of the imprint signature was observed in the 4 frozen and the 2 FFPE TLS– tumors (Data S2), with the exception of one tumor

(a\_1) in which the gene signature identifies a small region expressing the *MZB1* PC-associated gene (Andreani et al., 2018) and *IGHG1*, although no TLS was observed by H&E staining and CD3-CD20 IF labeling (Data S2, page 10).

The dominance of Ig and B cell-associated genes in the TLS imprint signature prompted us to focus on B cells. We first aimed to precisely locate transcriptionally distinct B cell subtypes with regard to TLS. Using robust cell type decomposition (RCTD) (Cable et al., 2021) to spatially map B cell subsets defined in single cell analyses of tonsillar B cells (King et al., 2021), we found scarce expression of naive B cell-associated genes (Figure 2D) and a strong association of FCRL4+ memory B cells ( $p < 2e-16$ ), GC B cells ( $p = 0.0087$ ) and plasmablasts ( $p = 2e-16$ ) signatures with TLS (Figures 2D and S2C). Expression of the PC-associated gene *MZB1* was high in TLS and globally low in the tumor area ( $p = 2e-16$ ) (Figure S2C) of the illustrated frozen tumor. We found similar results in the illustrated FFPE tumor (Figures 2I and S2D). However, numerous dispersed spots with expression of *MZB1*

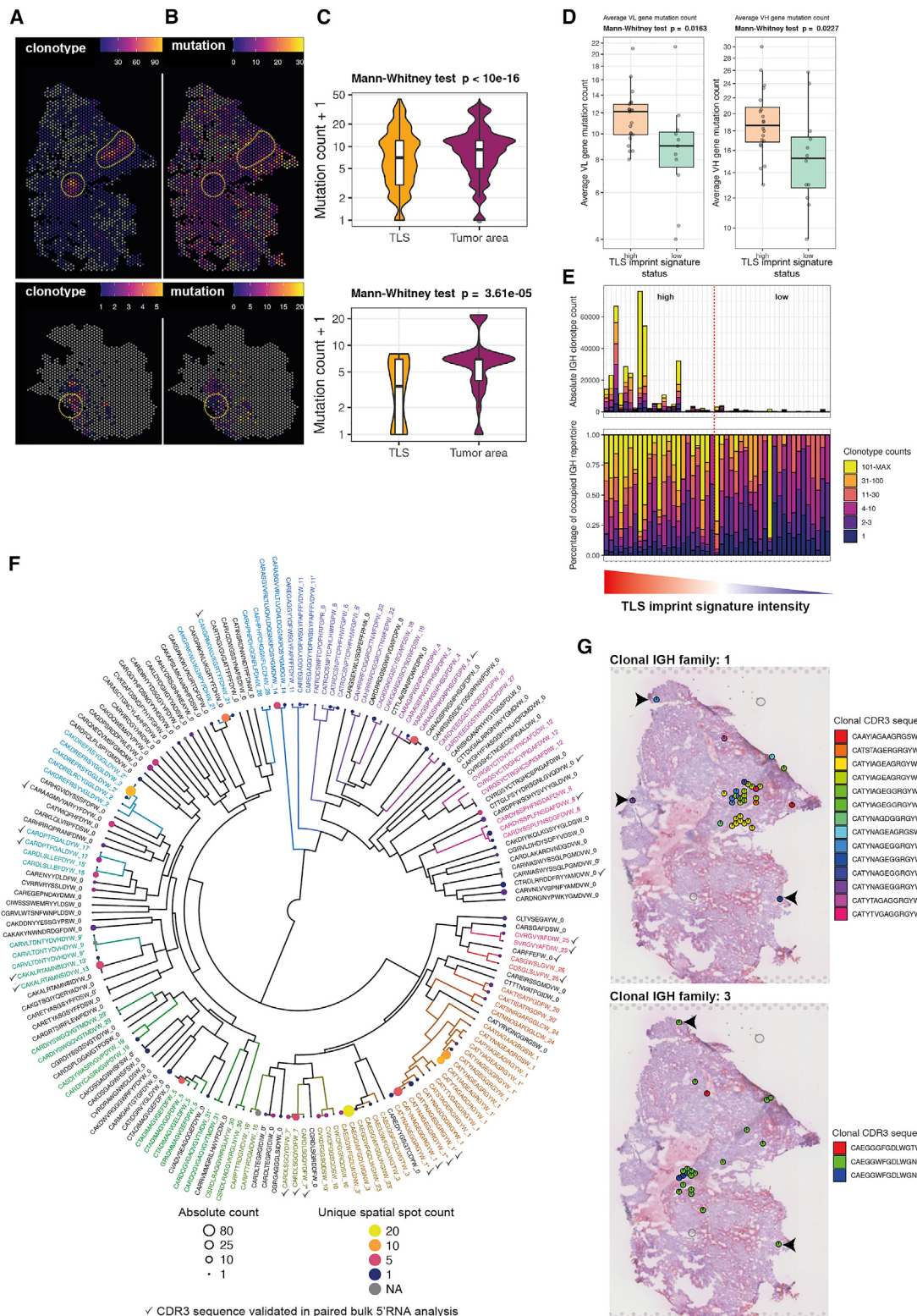


**Figure 3. Spatial BCR profiling identifies somatic hypermutation and clonal amplification occurring in TLS+ areas and propagation of selected clones in the tumor zone**

Bulk BCR profiling validating mutated and expanded repertoire in TLS+ tumors.

(A) Spatial distribution of the average number of unique IGL clonotypes per spot for 2 TLS+ tumors. (B) Spatial distribution of the average VL mutation counts per spot.

(legend continued on next page)

located at distance from TLS were detected in different locations within the tumor (Figures 2D and 2I; Data S2). *MZB1* is part of the plasmablast signature and is highly expressed in PCs (King et al., 2021). Since plasmablasts were confined to TLS areas, (Figures 2D and 2I) and a high expression of *MZB1* was found outside TLS, it is likely that *MZB1* expressing PCs were present not only in the TLS but also in the tumor beds. Owing to the PC's main function of producing antibodies, we analyzed the spatial expression of immunoglobulin genes. *IGHM* was almost exclusively expressed in TLS areas ( $p < 2e-16$ ), reinforcing the presence of non-switched B cells within TLS, whereas *IGHG1*, *IGHA1*, and pan Ig (geometric mean of *IGKC* and *JCHAIN*) genes were highly expressed in TLS areas ( $p < 2e-16$ , respectively) but also at distance in the tumors (Figures 2E, 2J, S2C, and S2D; Data S2). The dispersed expression of *IGHG1* and *IGHA1* suggests that isotype-switched PCs have been formed in TLS and disseminate at distance (Figures 1C, 1F, 2E, and 2J; Data S2).

Strikingly, high expression of the pan fibroblast marker *COL1A1*, together with the MCP-counter fibroblastic signature, were found at the same location as pan Ig genes (*IGKC*, *JCHAIN*, *IGHG1*, and *IGHA1* genes (Figures 1C, 1F, 2E, and 2J; Data S2). Since it has been reported that *CXCL12* is associated with PC migration and retention in PC niches located in the bone marrow (Chang et al., 2018), medullary cords of lymph nodes (Huang et al., 2018), and chronically inflamed tissues (Lindquist et al., 2019), we analyzed *CXCL12* expression and found that it co-localized with that of *MZB1* (Figure S4A).

To further evaluate the spatial co-location between these different signatures, the expression of each signature was dichotomized using the median as a cutoff to define "high" or "low" expression categories for each spot. When a gene was shared by two signatures, it was removed from one of them to avoid its influence on the statistical analyses. Thus, we removed *MZB1* from the TLS imprint signature for the analysis of TLS/*MZB1* overlap and *CXCL12*, when we analyzed the overlap between TLS and *CXCL12* gene expressions (see STAR Methods). Meaningful overlap was then assessed by computing Chi-square test between signatures taken two by two and highlighting spots classified as "high/high" in yellow. This analysis not only confirmed co-localization of the TLS signature with *MZB1*, fibroblasts, and *CXCL12* ( $p < 2e-16$ ) but also co-localization of fibroblasts with *CXCL12* ( $p < 2e-16$ ), *MZB1* with fibroblasts ( $p < 2e-16$ ), and *MZB1* with *CXCL12* ( $p < 2e-16$ ) at distance from TLS (Figure S4A). These co-localizations were confirmed in the other TLS+ tumors (two are illustrated in Figures S4B and S4C) whereas minor to no associations were observed in TLS- tumors (Figures S4D and S4E). Overall, we concluded

that in TLS+ tumors, *IGHG1* and *IGHA1* expressing PCs are present in the TLS vicinity and may disseminate within the tumor in association with fibroblasts.

### Spatial B cell receptor (BCR) profiling identifies *in situ* hypermutation and clonal selection

The co-localization of B cell maturation subtypes and PCs in TLS hinted at an *in situ* B cell adaptive immunity generation. During such process, B cells mutate their B cell receptor (BCR) sequence, and the most affine clones are selected and expanded. To evidence these events, it is necessary to study the nucleotideic sequence of BCRs. The Visium spatial technology is based on RNA sequencing of barcoded transcripts, which allowed us to access the raw transcripts and perform spatial BCR repertoire profiling. We used the publicly available implementation MiXCR (Bolotin et al., 2017), a tool designed to identify BCR IgL and IgH clonotypes and their germline somatic hypermutations from 5' RNA sequencing data, as well as the commercially available 3' Frozen Visium kit, which allowed us to obtain mRNA transcripts of sufficient length to capture the full complementary determining region (CDR3) regions of most IgL and some IgH sequences. This capture was facilitated by sequencing with 3 times the recommended depth (150,000 reads per spot, which corresponds to 225 million reads per sample). MiXCR identified a number of unique clonotypes: a total of 3,015 lambda light chains, 3,084 kappa light chains, and 325 heavy chains. The highest number of unique clonotypes and total Ig counts were found in TLS+ tumors (Table S2). The highest numbers of unique light chain clonotypes were also found in TLS areas (Figure 3A). B cell maturation was evaluated by measuring the mutational counts of V regions of Ig light chain sequences compared with the mapped V germline gene. Median V gene mutational count showed low to median levels in the TLS areas and, strikingly, mostly highly mutated sequences at distance from TLS in the tumor area (Figure 3B). Nonetheless, the full range of mutations, including highly mutated sequences, was measured in TLS areas, whereas most Ig transcripts at distance from TLS were enriched in highly mutated sequences (for tumors presented in Figure 3B, median TLS mutations were 6 and 2.5; median tumor area mutations were 8 and 6, respectively,  $p < 10^{-4}$ ) (Figures 3B and 3C), indicating that somatic hypermutation occurs in TLS and suggesting that mutated PCs disseminate throughout the tumors. We investigated both light and heavy chain-mutation count in bulk 5' RNA-seq from 47 ccRCC tumors (including the 12 frozen tumors profiled by Visium) (Table S1), which were classified as TLS high or low using the median expression of the TLS imprint signature. The overall somatic hypermutation level was significantly higher in TLS-high versus TLS-low tumors, both for

(C) Distribution of VL mutation counts between the TLS and tumor area.

(D) Distribution of the average mutation counts of VL and VH genes between the TLS-high and TLS-low samples estimated from bulk 5' RNA-seq ( $n = 47$ ).

(E) Bar plots ordered according to the TLS imprint signature expression, showing the differential distribution of IGH clonotype counts between TLS-high and TLS-low tumors. Upper panel shows absolute values, lower panel shows relative values ( $n = 47$ ).

(F) CDR3 distance tree reconstructing clonal relationships between IGH clonotypes. Each IGH clonotype is identified by its CDR3 amino-acid sequences and the clonal family it belongs to (0: not clonal, 1–32: clonal). Colored branches and texts mark clonal families, black color indicates single sequences. Size of the dots represents the number of counts for each clonotype, and the color of the dot represents the number of different spatial spots in which the clonotype has been counted. Check marks (✓) identify CDR3 sequences that have been found in both spatial and bulk analyses from the same tumor (F and G).

(G) Spatial localization of IGH clonotypes belonging to two clonal families. Black arrows indicate clonal IGH clonotypes most distantly located from the TLS (up to 3 mm for both clonal families 1 and 4) in the tumor bed.

$p$  values were determined by two-sided Mann-Whitney tests.

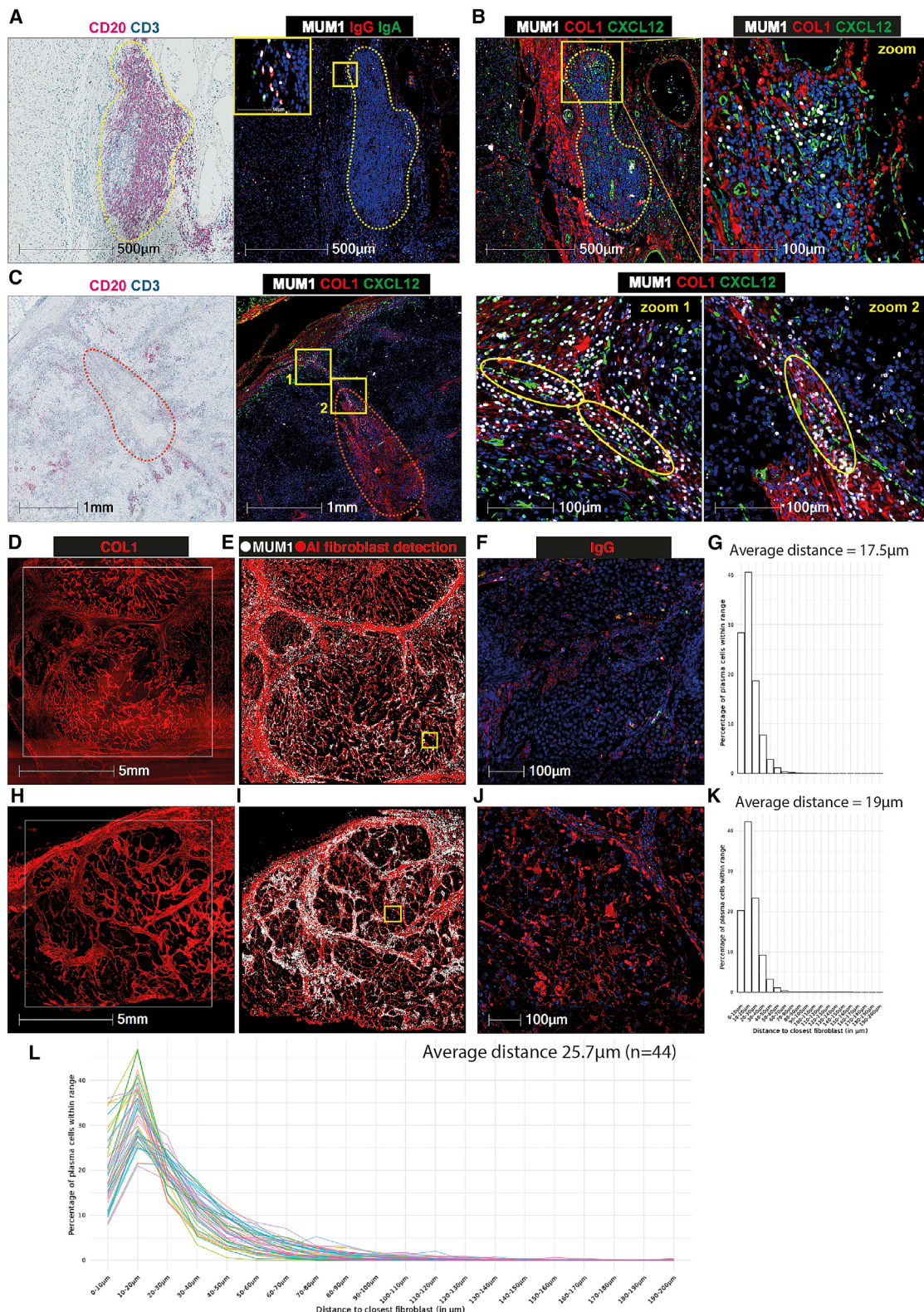


**Figure 4. Co-localization of PCs with fibroblasts and IgG tumor staining in the TLS+ tumors**

(A) Left, identification of the TLS by CD3 (green) and CD20 (red) chromogenic staining on one tumor. Right, staining of IgG+ (red), IgA+ (green), and MUM1+ (white) PCs in and around the TLS area. TLS area is highlighted by yellow dashed lines and zooms by yellow squares.

the VL (median TLS high = 12 mutations, median TLS low = 8 mutations,  $p = 0.0163$ ) and VH genes (median TLS high = 19 mutations, median TLS low = 13.5 mutations,  $p = 0.0227$ ) (Figure 3D). To determine whether somatic hypermutation was accompanied by clonotype selection, we investigated the IgH repertoire of the bulk 5' RNA-seq data. The repertoire of TLS-high samples exhibited both a large number of total clonotype counts as well as a higher proportion of clonotypes counted more than 100 times (Figure 3E). Indeed, 30% of the repertoire of TLS-high tumors were occupied by clonotypes identified over 100 times versus 1% in the TLS-low tumors ( $p = 10e-7$ ), revealing an ongoing immune response in TLS-high samples. Inversely, TLS-low samples showed less diverse repertoires, with lower counts and most being measured less than 10 times (Figure 3E), except for one tumor which had 123 IgH clonotypes and only 2 counted over 100 times (Figure 3E).

Finally, to determine the clonal relationships and location of amplified IgH clonotypes, we performed clonality assessment on the 3' RNA-seq spatial data. Clonality was defined by the same family of VH genes, identical JH genes and the same CDR3 length and a maximum divergence of 15% in the CDR3 nucleotidic sequences between VH sequences. To visualize these relationships, we computed the Levenshtein distance between each VH CDR3 sequence, and represented it with a circular tree for a TLS+ tumor (id: b\_1). In total, 31 clonal families with 2 to 16 unique members were identified (Figure 3F). Within one family, some clones could be detected up to 80 times and in up to 20 different spatial locations (Figure 3F). Localization of IgH clonotypes on the Visium slide evidenced clonotypes of the same family clustered in the vicinity of TLS and sparsely disseminated at distance, illustrated by clonal IgH families 1 and 3 (Figure 3G black arrows). Some clonotypes could even be detected at up to 3 mm from the TLS area where they might have been generated (Figure 3G, clonal family 1, clonotype CATYNAGEGGGRGYW\_1 and clonal family 3, clonotype CAEGGWFGDLWGNW\_3). To confirm these results, we looked for CDR3 nucleotidic sequences of clonotypes identified from spatial 3' RNA transcriptomics in clonotypes inferred from paired bulk 5' RNA-seq. On tumor b\_1, we validated the presence of 15 IGH CDR3 sequences out of 169, identified by a tick mark on Figure 3F. Clonotypes with the CDR3 sequence CATYNAGEGGGRGYW of clonal family 1, identified by black arrows on Figure 3G, were also found in bulk 5' RNA-seq data, thus confirming our result. Moreover, these clonotypes were located both inside and at distance from TLS, suggesting the migration of the corresponding B cell clones.

In TLS-low samples, the number of detected clonotypes was very low (Table S2), preventing the analysis of Ig transcripts and also supporting the proposition that intra-tumoral PCs are mostly generated in TLS. Altogether, these data support an

*in situ* TLS-mediated maturation, allowing for selection, clonal amplification, and dissemination of selected PCs in various areas of the tumors.

### Plasma cells disseminate from TLS along fibroblastic tracks

To analyze the location of intra-tumoral PCs and fibroblasts and the expression of CXCL12 *in situ*, we used multiplex IF labeling of FFPE tumor sections, utilizing multiple myeloma oncogene 1 (MUM1) (IRF4) as a specific marker for PCs and COL1 (Col1a1) for fibroblasts. Double positive MUM1+ IgG+ PCs and a few MUM1+ IgA+ PCs were detected within TLS areas were defined by chromogenic CD3/CD20 labeling on a consecutive slide (Figure 4A). COL1+/CXCL12+ fibroblasts were observed juxtaposing MUM1+ PCs in these areas (Figure 4B). Moreover, alignments of PCs along fibroblastic tracks, embedded in a dense network of COL1+ CXCL12+ fibroblasts, were evidenced at distance from TLS (Figure 4C, zoom 1,2), thus demonstrating their dissemination in the tumor bed. To quantitatively evaluate the spatial relationships between PCs and fibroblasts, we performed AI detection of fibroblast nuclei on DAPI/MUM1/IgG/IgA IF stained samples, as shown in Figure S5. As illustrated in Figure 4, the detection of fibroblast nuclei mapped the COL1+ fibroblastic tracks (Figures 4D, 4E, 4H, and 4I). The vast majority of PCs were in very close proximity to fibroblasts nuclei, with an average distance of 17.5 and 19  $\mu\text{m}$  for the two tumors for which the distance distribution is presented in Figures 4G and 4K. An average distance of 25.7  $\mu\text{m}$  was measured on 44 tumor samples (Figure 4L). Altogether, these data recapitulate the co-expression of Ig and fibroblast transcripts, as well as the co-expression of fibroblast transcripts and CXCL12 (Figure 2E) and validate the location of PCs within the TLS and along fibroblastic reticular cell (FRC) tracks identified by spatial transcriptomics. Strikingly, IgG bound to tumor cells was detected in tumoral nests surrounded by MUM1+ IgG+ fibroblastic tracks (Figures 4F and 4J).

### TLS and Ig-producing PCs are associated with IgG antibodies bound to apoptotic tumor cells and with response to immunotherapy

To further investigate the link between TLS, and intra-tumoral PCs, and Ig staining, we first analyzed TLS maturity. Mature TLS were characterized by GC containing a B cell zone surrounded by a T cell zone, in which CD4<sup>+</sup>PD1<sup>+</sup> T cells, CD4<sup>+</sup> PD1<sup>+</sup>CXCR5<sup>+</sup> Tfh cells, and CXCL13-producing cells were present (Figure 5B). The GC zone was characterized by a network of CD23<sup>+</sup> follicular dendritic cells (FDC), BCL6<sup>+</sup> CD20<sup>+</sup> B cells, and PNAd<sup>+</sup> HEVs being detected at the periphery (Figure 5C). We investigated the correlation between the presence of TLS and the density of PCs in 103 tumors. Significant associations

(B) Left panel, co-localization of MUM1+ PCs (white), COL1+ fibroblasts (red), and CXCL12+ reticular cells (green) in the TLS. Right, zooms of the yellow squares from left panel showing PC alignment along trajectories of CXCL12+ reticular cells with COL1+ segments.

(C) Tumor area of a TLS+ tumor (left) showing a PC alignment along COL1+ CXCL12+ fibroblastic tracks (red and green). Zones 1 and 2 are zooms on the threads of PCs closely contained along COL1A+ CXCL12+ fibroblastic tracks.

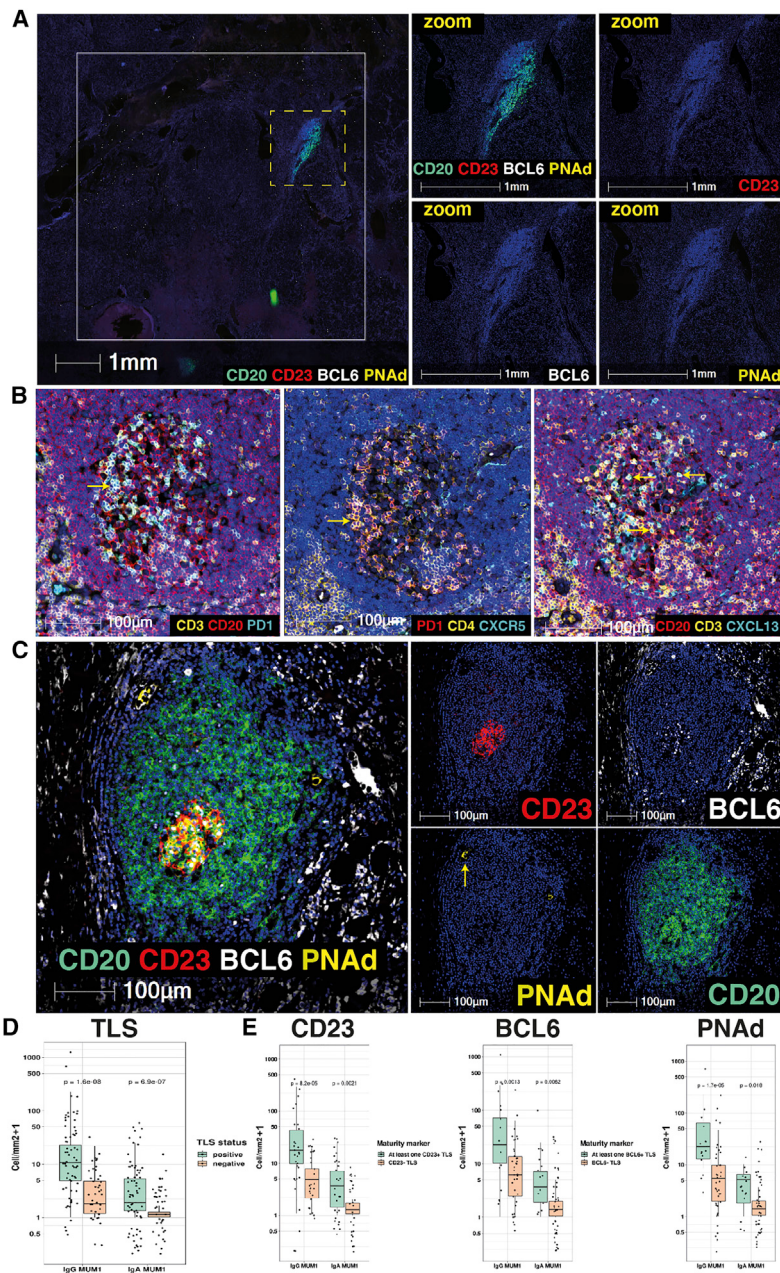
(D and H) COL1A staining of two tumors identifying fibroblastic tracks, white square highlights the area analyzed by AI.

(E and I) AI-based detection of fibroblast nuclei (red) and MUM1+ PC detection by IF (white).

(F and J) Zoom of the yellow squares from (E and I) showing IgG tumoral staining inside tumor nests.

(G and K) Histograms of distances between MUM1+ PCs and AI-based detection of fibroblast nuclei for tumors illustrated in (E and I), respectively.

(L) Distribution of the distances between MUM1+ PCs and AI-based detection of fibroblast nuclei for 44 tumors.



between the presence of TLS and the densities of MUM1+ IgG+ cells (median in TLS+ tumors = 10 cells/mm<sup>2</sup>, median in TLS- tumors = 1 cell/mm<sup>2</sup>,  $p = 1.6e-8$ ) and MUM1+ IgA cells (median TLS+ tumors = 1 cell/mm<sup>2</sup>, median TLS- tumors = 0 cell/mm<sup>2</sup>,  $p = 6.9e-7$ ) were observed (Figure 5D). We further investigated the correlation of TLS maturity markers with the density of MUM1+IgG+ and MUM1+IgA+ PCs on the 57 TLS+ samples. We found strong correlations between the presence of TLS containing CD23<sup>+</sup> FDC network, BCL6+ cells, and PNAd+ HEVs with MUM1+IgG+ PC and MUM1+IgA+ PC densities (Figure 5E).

The high densities of Ig-producing PCs detected around tumor nests and the observation of IgG in tumor nests prompted us to investigate for the presence of anti-tumor antibodies (Figures 4F and 4J). Of note, a bright labeling of CAIX+ tumor cell membrane

**Figure 5. Mature TLS+ tumors display more switched MUM1+ PCs**

(A) Multiplex immunofluorescence labeling of a tumor with an immature TLS. CD20<sup>+</sup> B cells (green) and negative for CD23<sup>+</sup> follicular dendritic cells (red), BCL6<sup>+</sup> GC B cells (white), and PNAd+ HEVs (yellow). White square identifies the Visium capture area for the tumor c\_20 analyzed by Visium for FFPE.

(B) Detection of T follicular helper cells (arrows) inside TLS: CD3<sup>+</sup> PD1<sup>hi</sup> (left panel), CD4<sup>+</sup> CXCR5+PD1+ cells (middle panel), and CD3<sup>+</sup> CXCL13+ cells (right panel).

(C) Markers of TLS maturity. CD23<sup>+</sup> follicular dendritic cells (red), BCL6<sup>+</sup> GC B cells (white), and PNAd+ HEVs (yellow).

(D) Densities of IgG+ (left) and IgA+ (right) MUM1+ PCs according to TLS presence ( $n = 103$ ).

(E) Densities of IgG+ and IgA+ MUM1+ PCs according to TLS maturation markers ( $n = 57$ ).

$p$  values were determined by two-sided Mann–Whitney tests.

by conjugated anti-human IgG was observed as illustrated in a TLS+ tumor, whereas no labeling was observed in a TLS- tumor (Figure 6A). Its subsequent quantification on 103 tumors revealed high percentages of IgG positivity, reaching up to 100% of tumor cells in TLS+ as compared with TLS- tumors (median = 70% and 30%, respectively,  $p = 0.0046$ ) (Figure 6B; Table S3). A weak IgA labeling was observed in both TLS+ and TLS- tumors (Figure 6F; Table S3). Furthermore, a significant association was found between IgG labeling on tumor cells and infiltration of tumors with MUM1+ IgG+ PCs (median IgG labeling of MUM1+IgG+ high tumors = 80%, and of MUM1+IgG+ low tumors = 40%,  $p = 0.000195$ ) (Figure 6C), with IgA labeling being very low (Figure 6D).

To unveil potential functions of tumor-bound IgG antibodies, we searched for signs of apoptosis occurring in tumor cells,

identified by their typical large nucleus and clear-cell phenotype, using an antibody that detects cleaved caspase 3. Figure 6E illustrates labeling of cleaved caspase 3 in a TLS+ and a TLS- tumor. The density of cleaved caspase 3+ tumor cells was significantly higher in tumors with IgG staining above 60%, which is the mean value that discriminates best two tumor populations (Figure 6F), than in tumors with less than 60% IgG+ tumor cells (median: 12.7 cells/mm<sup>2</sup> and 7.2 cells/mm<sup>2</sup> respectively,  $p = 0.0255$ ).

We addressed the question of the mechanisms that may be at work in inducing apoptosis of tumor cells. Since macrophages and NK cells are the main effectors of antibody-dependent cellular cytotoxicity (ADCC), we evaluated the overall density of CD68<sup>+</sup> macrophages and NKP46<sup>+</sup> NK cells on 76 and 98 tumors, respectively (Table S3), and found no correlation with the density of

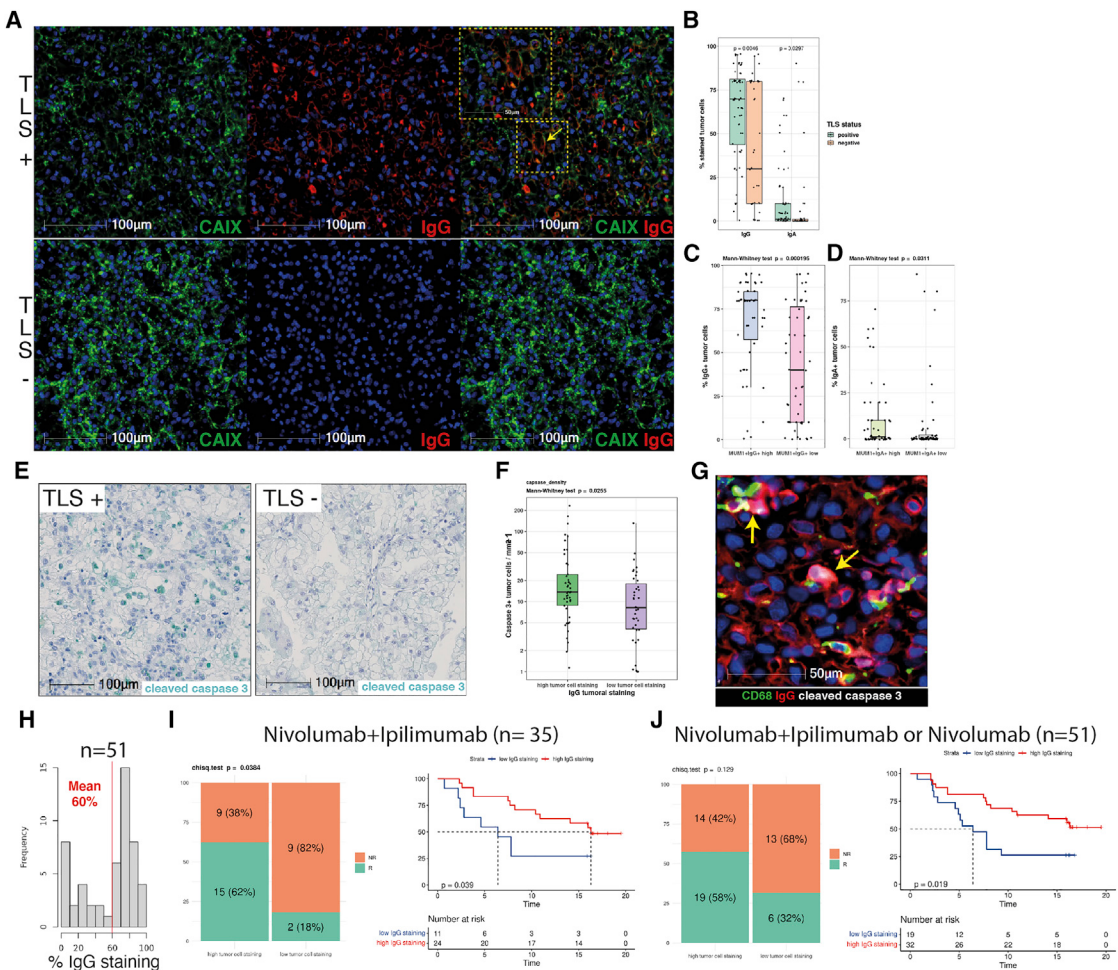


**Figure 6. Tumors with TLS present increased IgG+ CAIX+ tumor cell staining compared with tumors with immature or no TLS. Association with tumor cell death and response to ICI.**

(A) Upper panel, CAIX+ (green) and IgG+ (red) stained tumor cells of a TLS+ tumor. Lower panel, CAIX+ IgG-stained tumor cells of a TLS– tumor. Yellow dotted square and arrow indicate double positive cells.

(B) Percentage of IgG+ (left) and IgA+ (right) tumor cells according to TLS status ( $n = 103$ ).

(C) Percentage of IgG+ tumor cells according to densities of MUM1+ IgG+ PCs ( $n = 103$ ).

(D) Percentage of IgA+ tumor cells according to densities of MUM1+ IgA+ PCs ( $n = 103$ ).

(E) Cleaved caspase-3 (green) chromogenic staining indicating ongoing apoptosis in tumor cells for a TLS+ (left) and a TLS– (right) tumor.

(F) Cleaved caspase-3 positive tumor cell density (cell/mm<sup>2</sup>) according to the mean of IgG+ tumor cell staining ( $n = 103$ ).

(G) Co-localization of CD68+ macrophages with IgG+ cleaved caspase-3+ tumor cells.

(H) Distribution of IgG tumor staining and definition of the mean as cutoff (mean = 60%,  $n = 51$ ).

(I) Response rates and progression-free survival (in months) of patients treated by Nivolumab + Ipilimumab stratified on the percentage of IgG+ tumor cells.

(J) Response rates and progression-free survival (in months) of patients treated by either Nivolumab + Ipilimumab or Nivolumab stratified on the percentage of IgG+ tumor cells.

(B-D and F) p values were determined by two-sided Mann-Whitney tests. (I and J) Analyses performed with Kaplan-Meier estimates and two-sided log-rank tests.

cleaved caspase-3+ tumor cells (data not shown). However, we found that tumors with both high numbers of apoptotic cells and a high percentages of IgG-stained tumor cells were more infiltrated by CD68+ macrophages than tumors with high numbers of apoptotic cells but low percentages of IgG-stained tumor cells ( $p = 0.0054$ ) (Figure S6A). Proximity assessment evidenced a positive correlation between CD68+ macrophages and cleaved caspase 3+ tumor cells on 14 tumors, with high numbers of apoptotic cells and high percentages of IgG-stained tumor cells ( $r = 0.557$ ,

$p = 8.21 \times 10^{-6}$ ) (Figure S6B). NK cells were present at lower densities than macrophages (Table S3), and did not exhibit such correlations (Figures S6C and S6D). Moreover, we found a median value of 13.6% apoptotic tumor cells located at less than 25 μm of a macrophage, whereas we did not observe close proximity between NK cells and apoptotic tumor cells (median = 0.5%) (Figure S6E). Figure 6G illustrates the close proximity between CD68+ macrophages and IgG-stained/cleaved caspase 3+ tumor cells.

To evaluate the impact of IgG tumoral staining on ICI treated patients, we evaluated the available 35 tumors from NI treated patients and 16 from Nivolumab-treated patients (one Nivolumab-treated patient had non-evaluable IgG tumoral staining and one had missing clinical information). We chose the mean IgG tumoral staining (60%) as the cutoff, as it discriminated best two populations of tumors (Figure 6H). For NI treated patients, we evidenced a significant association between therapeutic responses with 62% objective responses (OR: complete and partial responses) in patients with IgG tumoral cell labeling above the mean, as compared with 18% OR with IgG tumoral labeling below the mean ( $p = 0.0384$ ), as well as a significantly longer PFS of patients with high IgG tumoral cell staining compared with low IgG tumoral cell staining (median PFS = 16.3 months versus 6.4 months,  $p = 0.039$ ) (Figure 6I). The cohort of patients treated by Nivolumab alone was too small for statistical analysis. However, among the 51 patients treated by ICI, either Nivolumab alone, or NI, a significantly longer PFS was observed for patients with high tumoral staining (not reached versus 6.4 months,  $p = 0.019$ ), with a trend for a higher number of OR (58% versus 32%) (Figure 6J).

## DISCUSSION

This study performs a comprehensive analysis of B cell differentiation into antibody secreting cells *in situ* in the TME. Integration of spatial transcriptomics, bulk RNA-seq, and multicolor IF enables us to demonstrate that TLS are sites for maturation, selection, clonal amplification, and isotype switching of B cells, and that clonal PCs generated within TLS can migrate at distance in the tumor, guided by CXCL12-positive fibroblasts.

To spatially visualize TLS areas by transcriptomics, we identified genes for which expression was higher in the TLS areas, confirmed by CD3-CD20 IF staining, than in the rest of the tumor. It yielded a 29-gene signature that is dominated by Ig genes highly expressed in PCs. Since PCs are Ig-producing factories, it is not surprising that their presence is revealed by the high expression of Ig genes, including genes (*IGHA*, *IGHG1*, *IGHG2*, *IGHG3*, *IGHG4*) in which high expression demonstrates isotopic switching. The signature proposed here does not aim to characterize TLS but to measure their imprint on the dominant transcriptomic features in tumors. It allowed us to precisely visualize the transcriptomic distribution of B cell- and PC-associated genes and their spatial relationships with fibroblast-associated genes. It was also used to discriminate, at its median expression, between TLS-high and -low tumors for the bulk RNA analyses of the B cell repertoires. Since Tfh cells are found in TLS and participate in B cells activation in GC (Gu-Trantien et al., 2013; Vinuesa et al., 2016), a Tfh-derived signature and particularly CXCL13 produced in Tfh (Gu-Trantien et al., 2017), have been used as markers for TLS presence in breast (Gu-Trantien et al., 2013) and colorectal (Becht et al., 2016c) cancers, as well as soft tissue sarcoma (Petitprez et al., 2020) and melanoma (Helminck et al., 2020). A 12-chemokine signature correlating with the presence of TLS was proposed in colorectal cancer (Coppola et al., 2011) and used in hepatocellular carcinoma (Calderaro et al., 2018; Meylan et al., 2020), melanoma (Messina et al., 2012), and for The Cancer Genome Atlas (TCGA) survey of different

types of cancers (Sautès-Fridman et al., 2019). High expression of this signature correlated with that of B cell and fibroblast signatures measured by MCP-counter (Tokunaga et al., 2020). However, none of these signatures was derived from transcriptomically resolved analysis and, although useful to assess for TLS presence, it does not take into account the dominant transcriptomic features imprinted by TLS in their vicinity and at distance in the tumors.

MCP-counter analysis of immune cell types in tumors analyzed by spatial transcriptomics revealed the unique distribution of B cell-associated genes signature in clusters containing several hot spots associated with TLS, contrasting with the diffuse distribution of CD8 T cells and myeloid cells. The expression of PC genes (*MZB1* and *IGKC*) and proteins (IgG, IgA, and MUM1) were detected not only in TLS-B cell rich areas but also at a distance. Maturation of B cells *in situ* was demonstrated by the increased V gene hypermutation load observed in B cells in the tumor area compared with TLS. Amplification is supported by the high repertoire occupancy of some clones in TLS+ tumors and selection by intra-clonal diversification of B cells within and outside TLSs. Spatial transcriptomics by 10 $\times$  Visium technology allows the quantification of gene expression levels on whole tissue sections. Sequences of immunoglobulin transcripts can be accessed and IGH and IGL clonotypes can be identified. However, the use of 3' library technology might introduce PCR errors in the CDR3 region used for BCR profiling. These errors should be randomly distributed. Since we found the exact same sequences in several contiguous spots within the TLS and at distance, it seems very unlikely that the same error would be reproduced several times. Moreover, we ruled out this bias in our spatial clonotype localization since we found the exact same CDR3 nucleotidic sequence in clones identified by spatial transcriptomics and 5' bulk RNA-seq from the same tumors, as illustrated in Figure 3F.

The detection of the same IGH clonotypes inside TLSs and at distance supports the dissemination of TLS-generated PCs into the tumor beds. In addition, our study unravels an association of CXCL12 with this process, both in TLS and outside. Indeed, co-occurrence of expression of fibroblasts signature and CXCL12 with TLS imprint signature and the presence of COL1+CXCL12+ cells within TLS were detected both by spatial transcriptomics and multiplex IF, respectively. These TLS-located CXCL12+ fibroblastic cells may correspond to the CXCL12+ reticular cells found in mouse lymph node GCs (Malhotra et al., 2012; Rodda et al., 2015, 2018), where they facilitate the localization of CXCR4+ GC B cells for proliferation and somatic hypermutation (Silva-Cayetano and Linteman, 2020). In addition, fibroblast gene signatures also co-localized with the expression of PC genes in tumor areas located at distance from TLS. Multiplex IF also revealed PC distribution in linear tracks and in clusters along CXCL12+ COL1+ fibroblasts in tumor beds. Moreover, AI analysis established that PCs were in close proximity to fibroblasts around and inside tumor beds. These CXCL12+ COL1+ fibroblasts have common properties with the CXCL12 secreting follicular reticular cells (Chang et al., 2018), or mesenchymal stromal cell-like fibroblasts (Baryawno et al., 2019) found in the bone marrow, promoting long-term survival of memory PCs. Moreover, these cells support the survival of early PCs and their exit from the GC (Huang et al., 2018; Malhotra et al., 2012) in the

medullary reticular cells present in lymph nodes, as well as in chronically inflamed tissues (Buechler et al., 2021; Perez-Shibayama et al., 2019). Altogether, our study highlights the role of fibroblasts producing CXCL12 for the dissemination and maintenance of PCs from TLS deeper into the tumor, in close contact with tumor cells. In addition, our data are consistent with early studies showing that murine PCs, as compared with B cells, downregulate CXCR5—the receptor for CXCL13—and upregulate CXCR4—the receptor for CXCL12—and migrate in response to CXCL12 and not CXCL13 (Hargreaves et al., 2001).

Previous studies have shown that mature TLSs are composed of a T cell zone, in which naive T cells are activated to become memory and effector T cells (de Chaisemartin et al., 2011; Goc et al., 2014), and a GC containing B cell follicles, in which Tfh cells activate B cell differentiation (Garaud et al., 2019), leading to the presence of memory activated GC subsets and PCs (Garaud et al., 2019; Germain et al., 2014; Helmink et al., 2020; Kroeger et al., 2016). In the present work, we validated the presence of different maturation states of B cells within TLS and focused on the generation, maturation, clonal selection, and amplification of PCs occurring *in situ*, establishing them as the intra-tumoral sites of antibody-producing cells. This is in line with previous observations showing the presence of clonally expanded B cells and somatically mutated Ig genes by bulk repertoire profiling in tumors (Bolotin et al., 2017; Coronella et al., 2002; Iglesia et al., 2014; Nielsen et al., 2012; Saul et al., 2016) or in microdissected TLS (Cipponi et al., 2012; Nzula et al., 2003). It is also in accordance with reports showing infiltration of tumors with PCs in some cancer types (Biswas et al., 2021; Germain et al., 2014; Ito et al., 1986; Kroeger et al., 2016; Montfort et al., 2017; Weiner et al., 2021), correlating with TLS presence (Germain et al., 2014; Kroeger et al., 2016; Montfort et al., 2017).

Although we do not formally demonstrate that clonal B cells generated in TLSs lead to anti-tumor antibody production, we show that tumors harboring mature TLS are characterized not only by a PC-rich infiltrate, as evidenced by the positive correlation between CD23, BCL6, and PNAd labeling of TLS with IgG+ MUM1+ PCs but also by the high number of IgG-stained CAIX+ cells, supporting the proposition that TLS sustain the production of IgG antibodies reacting with tumor cells. Despite the detection of IgA-producing PCs, IgA-labeled tumor cells were found only in a small fraction of tumors ( $n = 7/103$ ) (Table S3). The presence of anti-tumor IgG has also been described in supernatants of tumor-infiltrating B cells in non-small cell lung cancer (NSCLC) (Germain et al., 2014), and IgG bound to tumor cells were reported in ovarian cancer (Montfort et al., 2017) and human papilloma virus (HPV)+ head and neck squamous cell carcinoma (HNSCC) (Wieland et al., 2021).

The mechanisms by which PCs generated in TLS and the antibodies they produce inhibit cancer progression (Sautes-Fridman et al., 2019), and their response to immunotherapies (Cabrita et al., 2020; Gao et al., 2020; Helmink et al., 2020; Petitprez et al., 2020; Vanhersecke, 2021) remain to be fully elucidated. PCs produce tumor-specific antibodies, creating antigen-antibody complexes that could be internalized by DCs and favor efficient antigen presentation to T cells (Kalergis and Ravetch, 2002). This process could result in amplification of T cell responses, thus synergizing with anti-checkpoint immunotherapy and therapeutic vaccines (Lutz et al., 2014; Maldonado et al.,

2014). Tumor cell bound antibodies may also locally activate effector responses by binding C1q, activating the complement pathway (Roumenina et al., 2019), and binding to Fc $\gamma$  receptors on NK cells and macrophages (Bournazos et al., 2020). We addressed the question of the effector role of these cells in tumor cell apoptosis. In tumors rich in apoptotic cells with high percentages of IgG-stained tumor cells, which may be targets for ADCC, we found higher macrophage densities than in apoptotic tumors with low percentages of IgG-stained cells. There were no differences for NK cells. Moreover, we found a significant proportion of cleaved caspase3+ tumor cells in close proximity to macrophages, but not to NK cells, in tumors with high densities of IgG-labeled tumor cells. It does not formally demonstrate that macrophages are indeed killing tumor cells, but it is an argument to suggest that they may act as effector cells through ADCC. The fact that NK cells do not seem to be associated with tumor cell killing may be due to their small densities in the ccRCC tumors that we analyzed as well as the fact that they are often in an exhausted state in many solid tumors (Russick et al., 2020). IgG-mediated macrophage killing of tumor cells may be one of the steps leading to efficient anti-tumor immunity. Indeed, even if only a small number of tumor cells were labeled with an antibody recognizing cleaved caspase 3 as a marker of dying cells, it should be sufficient to release antigen-forming immune complexes that amplify T cell reactions (Kalergis and Ravetch, 2002), diminishing the antigenic threshold necessary to allow a better therapeutic response to ICI (Fridman et al., 2021). The nature of the tumor cell membrane antigens binding IgG antibodies remains to be determined, as they may represent useful targets for innovative immunotherapies. There are scarce reports on the identification of such antigens. In NSCLC, mitogen-stimulated intra-tumoral B cells have been shown to produce IgA and IgG antibodies to an array of cancer testis antigens, but their presence in the patient's tumor cells was not demonstrated as well as the TLS origin of the B cells (Germain et al., 2014). Production of HPV specific IgG antibodies by tumor-infiltrating lymphocytes was evidenced in HNSCC (Wieland et al., 2021). In ovarian cancer, IgA was detected on tumor cells co-localizing with the polyIgReceptor (plgR), resulting in IgA transcytosis that sensitizes tumor cells to cytotoxic killing by T cells in an antigen-independent manner. IgA produced by thrombospondin-1 N-terminal domain (TSPN) and brain-derived neurotrophic factor BDNF-reactive immortalized B cells recognized these antigens on an ovarian cancer cell line and inhibited autologous tumor growth *in vivo* better than control IgA (Biswas et al., 2021). Our work was not directed toward antigen identification but demonstrates an active *in situ* process of TLS-driven PCs formation, which migrates in the tumor core, producing antibodies—particularly IgG—that recognize and bind to patient's tumor cells, initiating IgG-dependent anti-tumoral effector mechanisms.

Although our study was not designed to analyze the impact of these mechanisms, we strikingly found a significant correlation between the percentage of IgG-labeled tumor cells, a higher response to ICI, and subsequently a longer PFS, as observed in patients with ccRCC treated with the combination of Nivolumab and Ipilimumab, and confirmed on a cohort of the same patients supplemented with patients treated with Nivolumab alone from the BIONIKK trial, supporting the medical relevance of our data.

Our study has several limitations. Spatial transcriptomic analyses reveal the architecture of a limited part of a tumor and do not take into consideration potential 3D tumor heterogeneity. This limitation is inherent to this type of analysis; however, we validated our findings using imaging by IHC and multicolor IF, as well as with IgG labeling of tumor cells at other parts of the tumors using another tumor bloc. The Visium technology is built around 3' RNA capture, which is not the best fitted tool to study the BCR repertoire and may introduce PCR errors. We validated our findings by 5' bulk RNA-seq. Another limitation of our study is that, although we show that the percentage of IgG-stained tumor cells correlates with the density of IgG+PCs, it does not formally demonstrate that the latter produce *in situ* IgG antibodies recognizing tumor-associated antigens. The proximity of apoptotic IgG-coated tumor cells with macrophages suggests that the latter may act as effector cells through ADCC, but the mechanisms involved were not determined with certainty. Finally, the significant correlation between high numbers of IgG-labeled tumor cells and high response rate and PFS in ICI treated patients is established in one trial and awaits extension to other immunotherapy-treated patients with renal cell carcinoma (RCC) and other tumors.

Altogether, the present study demonstrated that the intra-tumoral generation of PCs in TLSs and the production of IgA and IgG antibodies associated with IgG binding to tumor cells will guide future therapeutic approaches. Inducing TLS in TLS-tumors or utilizing locally produced antibodies from immunotherapy responding patients may serve as novel therapeutic tools.

## STAR★METHODS

Detailed methods are provided in the online version of this paper and include the following:

- KEY RESOURCES TABLE
- RESOURCE AVAILABILITY
  - Lead contact
  - Materials availability
  - Data and code availability
- EXPERIMENTAL MODEL AND SUBJECT DETAILS
  - Ethics and patients
- METHOD DETAILS
  - Sample selection for the spatial transcriptomic assay
  - Bulk 5'RNA sequencing assay
  - Immunohistochemistry and immunofluorescence labelling assays
- QUANTIFICATION AND STATISTICAL ANALYSIS
  - Visium libraries pre-processing
  - Quantitative evaluation of TLS and cell densities
  - Artificial intelligence (AI) assisted spatial proximity analysis
  - Statistical analysis

## SUPPLEMENTAL INFORMATION

Supplemental information can be found online at <https://doi.org/10.1016/j.immuni.2022.02.001>.

## ACKNOWLEDGMENTS

We thank Simon Lefranc and François Xavier Huchet from the Centre de Ressources Biologiques (IMM, Institut Mutualiste Montsouris) for providing tumor samples and sections, Natalia Juiz and Mickael Ploquin (10X Genomics), and Christophe Klein from the Histology, cell imaging and flow cytometry platform (CHIC) from Centre de Recherche des Cordeliers for their help on this study. This work was supported by INSERM, Sorbonne Université, Université de Paris, Ligue Contre le Cancer (Equipe labellisée), CARPEM (Cancer Research for Personalized Medicine) program of the Sites Intégrés de Recherche sur le Cancer (SIRIC), Labex Immunooncology, INCa (HTE program), Cancéropôle Île-de-France, Association pour la recherche en thérapeutiques innovantes en cancérologie (ARTIC, BIONIKK contract [R17169DD], MM fellowship), and Foncer Contre le Cancer (fond de dotation).

## AUTHOR CONTRIBUTIONS

M.M., A.d.R., C.S.-F., and W.H.F. conceived the project and designed the study. M.M., A.d.R., C.S.-F., W.H.F., F.P., E.B., and C.-A.R. interpreted the results. A.B., I.G., G.L., A.C., and M.M. generated the spatial transcriptomic data. G.L. and J.V. generated the bulk RNA-seq data. M.M., F.P., and E.B. performed the computational analysis. A.B., I.G., G.L., and A.C. performed the IHC and IF assays. G.P. performed AI-based histopathological analyses. A.B., I.G., A.C., and C.S.-F. analyzed images. Y.-A.V., S.O., V.V., R.E., E.B., A.M., R.S.-S., P.L.-P., X.C., and C.-M.S. provided patient materials, clinical annotations, and medical insights. V.V. performed pathological reviewing of the H&E slides used for the spatial assay. M.M., A.d.R., C.S.-F., W.H.F., F.P., E.B., and C.-A.R. wrote the manuscript, which was reviewed by all authors.

## DECLARATION OF INTERESTS

The authors declare no competing interests.

Received: May 17, 2021

Revised: December 9, 2021

Accepted: February 2, 2022

Published: February 28, 2022

## REFERENCES

- Andreani, V., Ramamoorthy, S., Pandey, A., Lupar, E., Nutt, S.L., Lämmermann, T., and Grosschedl, R. (2018). Cochaperone Mzb1 is a key effector of Blimp1 in plasma cell differentiation and  $\beta$ 1-integrin function. *Proc. Natl. Acad. Sci. USA* **115**, E9630–E9639.
- Bannard, O., and Cyster, J.G. (2017). Germinal centers: programmed for affinity maturation and antibody diversification. *Curr. Opin. Immunol.* **45**, 21–30.
- Baryawno, N., Przybylski, D., Kowalczyk, M.S., Kfoury, Y., Severe, N., Gustafsson, K., Kokkaliaris, K.D., Mercier, F., Tabaka, M., Hofree, M., et al. (2019). A cellular taxonomy of the bone marrow stroma in homeostasis and leukemia. *Cell* **177**, 1915–1932.e16.
- Becht, E., de Reyniès, A., Giraldo, N.A., Pilati, C., Buttard, B., Lacroix, L., Selves, J., Sautès-Fridman, C., Laurent-Puig, P., and Fridman, W.H. (2016c). Immune and stromal classification of colorectal cancer is associated with molecular subtypes and relevant for precision immunotherapy. *Clin. Cancer Res.* **22**, 4057–4066.
- Becht, E., Giraldo, N.A., Lacroix, L., Buttard, B., Elaroui, N., Petitprez, F., Selves, J., Laurent-Puig, P., Sautès-Fridman, C., Fridman, W.H., et al. (2016a). Estimating the population abundance of tissue-infiltrating immune and stromal cell populations using gene expression. *Genome Biol* **17**, 218.
- Becht, E., Giraldo, N.A., Lacroix, L., Buttard, B., Elaroui, N., Petitprez, F., Selves, J., Laurent-Puig, P., Sautès-Fridman, C., Fridman, W.H., et al. (2016b). Erratum to: estimating the population abundance of tissue-infiltrating immune and stromal cell populations using gene expression. *Genome Biol* **17**, 249.
- Biswas, S., Mandal, G., Payne, K.K., Anadon, C.M., Gatenbee, C.D., Chaurio, R.A., Costich, T.L., Moran, C., Harro, C.M., Rigolizzo, K.E., et al. (2021). IgA

- transcytosis and antigen recognition govern ovarian cancer immunity. *Nature* 591, 464–470.
- Bolotin, D.A., Poslavsky, S., Davydov, A.N., Frenkel, F.E., Fanchi, L., Zolotareva, O.I., Hemmers, S., Putintseva, E.V., Obraztsova, A.S., Shugay, M., et al. (2017). Antigen receptor repertoire profiling from RNA-seq data. *Nat. Biotechnol.* 35, 908–911.
- Bolotin, D.A., Poslavsky, S., Mitrophanov, I., Shugay, M., Mamedov, I.Z., Putintseva, E.V., and Chudakov, D.M. (2015). MIXCR: software for comprehensive adaptive immunity profiling. *Nat. Methods* 12, 380–381.
- Bournazos, S., Gupta, A., and Ravetch, J.V. (2020). The role of IgG Fc receptors in antibody-dependent enhancement. *Nat. Rev. Immunol.* 20, 633–643.
- Buechler, M.B., Pradhan, R.N., Krishnamurty, A.T., Cox, C., Calviello, A.K., Wang, A.W., Yang, Y.A., Tam, L., Caothien, R., Roose-Girma, M., et al. (2021). Cross-tissue organization of the fibroblast lineage. *Nature* 593, 575–579.
- Cable, D.M., Murray, E., Zou, L.S., Goeva, A., Macosko, E.Z., Chen, F., and Irizarry, R.A. (2021). Robust decomposition of cell type mixtures in spatial transcriptomics. *Nat. Biotechnol.* <https://doi.org/10.1038/s41587-021-00830-w>.
- Cabrita, R., Lauss, M., Sanna, A., Donia, M., Skaarup Larsen, M.S., Mitra, S., Johansson, I., Phung, B., Harbst, K., Vallon-Christersson, J., et al. (2020). Tertiary lymphoid structures improve immunotherapy and survival in melanoma. *Nature* 577, 561–565.
- Calderaro, J., Petitprez, F., Becht, E., Laurent, A., Hirsch, T.Z., Rousseau, B., Luciani, A., Amaddeo, G., Derman, J., Charpy, C., et al. (2018). Intra-tumoral tertiary lymphoid structures are associated with a low risk of early recurrence of hepatocellular carcinoma. *J. Hepatol.* 70, 58–65.
- Chang, H.-D., Tokoyoda, K., and Radbruch, A. (2018). Immunological memories of the bone marrow. *Immunol. Rev.* 283, 86–98.
- Cipponi, A., Mercier, M., Seremet, T., Baurain, J.-F., Théate, I., van den Oord, J., Stas, M., Boon, T., Coulie, P.G., and van Baren, N. (2012). Neogenesis of lymphoid structures and antibody responses occur in human melanoma metastases. *Cancer Res* 72, 3997–4007.
- Coppola, D., Nebozhyn, M., Khalil, F., Dai, H., Yeatman, T., Loboda, A., and Mulé, J.J. (2011). Unique ectopic lymph node-like structures present in human primary colorectal carcinoma are identified by immune gene array profiling. *Am. J. Pathol.* 179, 37–45.
- Coronella, J.A., Spier, C., Welch, M., Trevor, K.T., Stopeck, A.T., Villar, H., and Hersh, E.M. (2002). Antigen-driven oligoclonal expansion of tumor-infiltrating B cells in infiltrating ductal carcinoma of the breast. *J. Immunol.* 169, 1829–1836.
- Courcier, J., de la Taille, A., Nourieh, M., Leguerney, I., Lassau, N., and Ingels, A. (2020). Carbonic anhydrase IX in renal cell carcinoma, implications for disease management. *Int. J. Mol. Sci.* 21, 7146.
- de Chaisemartin, L., Goc, J., Damotte, D., Validire, P., Magdeleinat, P., Alifano, M., Cremer, I., Fridman, W.-H., Sautès-Fridman, C., and Dieu-Nosjean, M.-C. (2011). Characterization of chemokines and adhesion molecules associated with T cell presence in tertiary lymphoid structures in human lung cancer. *Cancer Res* 71, 6391–6399.
- Dieu-Nosjean, M.-C., Goc, J., Giraldo, N.A., Sautès-Fridman, C., and Fridman, W.H. (2014). Tertiary lymphoid structures in cancer and beyond. *Trends Immunol* 35, 571–580.
- Fridman, W.H., Petitprez, F., Meylan, M., Chen, T.W.-W., Sun, C.M., Roumenina, L.T., and Sautès-Fridman, C. (2021). B cells and cancer: to B or not to B? *J. Exp. Med.* 218, e20200851.
- Gao, J., Navai, N., Alhalabi, O., Sieffker-Radtke, A., Campbell, M.T., Tidwell, R.S., Guo, C.C., Kamat, A.M., Matin, S.F., Araujo, J.C., et al. (2020). Neoadjuvant PD-L1 plus CTLA-4 blockade in patients with cisplatin-ineligible operable high-risk urothelial carcinoma. *Nat. Med.* 26, 1845–1851.
- Garaud, S., Buisseret, L., Solinas, C., Gu-Trantien, C., de Wind, A., Van den Eynden, G., Naveaux, C., Lodewyckx, J.-N., Boisson, A., Duvillier, H., et al. (2019). Tumor infiltrating B-cells signal functional humoral immune responses in breast cancer. *JCI Insight* 5, e129641.
- Germain, C., Gnjatic, S., Tamzalit, F., Knockaert, S., Remark, R., Goc, J., Lepelley, A., Becht, E., Katsahian, S., Bizouard, G., et al. (2014). Presence of B cells in tertiary lymphoid structures is associated with a protective immunity in patients with lung cancer. *Am. J. Respir. Crit. Care Med.* 189, 832–844.
- Goc, J., Germain, C., Vo-Bourgais, T.K.D., Lupo, A., Klein, C., Knockaert, S., de Chaisemartin, L., Ouakrim, H., Becht, E., Alifano, M., et al. (2014). Dendritic cells in tumor-associated tertiary lymphoid structures signal a Th1 cytotoxic immune contexture and license the positive prognostic value of infiltrating CD8+ T cells. *Cancer Res* 74, 705–715.
- Gu-Trantien, C., Loi, S., Garaud, S., Equeter, C., Libin, M., de Wind, A., Ravoet, M., Le Buanec, H., Sibleille, C., Manfouo-Foutsop, G., et al. (2013). CD4+ follicular helper T cell infiltration predicts breast cancer survival. *J. Clin. Invest.* 123, 2873–2892.
- Gu-Trantien, C., Migliori, E., Buisseret, L., de Wind, A., Brohee, S., Garaud, S., Noël, G., Dang Chi, V.L., Lodewyckx, J.-N., Naveaux, C., et al. (2017). CXCL13-producing TFH cells link immune suppression and adaptive memory in human breast cancer. *JCI Insight* 2, e91487.
- Hargreaves, D.C., Hyman, P.L., Lu, T.T., Ngo, V.N., Bidgol, A., Suzuki, G., Zou, Y.R., Littman, D.R., and Cyster, J.G. (2001). A coordinated change in chemo-kine responsiveness guides plasma cell movements. *J. Exp. Med.* 194, 45–56.
- Helmink, B.A., Reddy, S.M., Gao, J., Zhang, S., Basar, R., Thakur, R., Yizhak, K., Sade-Feldman, M., Blando, J., Han, G., et al. (2020). B cells and tertiary lymphoid structures promote immunotherapy response. *Nature* 577, 549–555.
- Huang, H.-Y., Rivas-Caicedo, A., Renevey, F., Cannelle, H., Peranzoni, E., Scarpellino, L., Hardie, D.L., Pommier, A., Schaeuble, K., Favre, S., et al. (2018). Identification of a new subset of lymph node stromal cells involved in regulating plasma cell homeostasis. *Proc. Natl. Acad. Sci. USA* 115, E6826–E6835.
- Iglesia, M.D., Vincent, B.G., Parker, J.S., Hoadley, K.A., Carey, L.A., Perou, C.M., and Serody, J.S. (2014). Prognostic B-cell signatures using mRNA-seq in patients with subtype-specific breast and ovarian cancer. *Clin. Cancer Res.* 20, 3818–3829.
- Ito, T., Saga, S., Nagayoshi, S., Imai, M., Aoyama, A., Yokoi, T., and Hoshino, M. (1986). Class distribution of immunoglobulin-containing plasma cells in the stroma of medullary carcinoma of breast. *Breast Cancer Res. Treat.* 7, 97–103.
- Gunderson, A.J., Rajamanickam, V., Bui, C., Bernard, B., Pucilowska, J., Ballesteros-Merino, C., Schmidt, M., McCarty, K., Philips, M., Piening, B., et al. (2021). Germinal center reactions in tertiary lymphoid structures associate with neoantigen burden, humoral immunity and long-term survivorship in pancreatic cancer. *Oncolimmunology* 10, 1900635.
- Kalergis, A.M., and Ravetch, J.V. (2002). Inducing tumor immunity through the selective engagement of activating Fc $\gamma$  receptors on dendritic cells. *J. Exp. Med.* 195, 1653–1659.
- Katoh, H., Komura, D., Konishi, H., Suzuki, R., Yamamoto, A., Kakiuchi, M., Sato, R., Ushiku, T., Yamamoto, S., Tatsuno, K., et al. (2017). Immunogenetic profiling for gastric cancers identifies sulfated glycosaminoglycans as major and functional B cell antigens in human malignancies. *Cell Rep* 20, 1073–1087.
- King, H.W., Orban, N., Riches, J.C., Clear, A.J., Warnes, G., Teichmann, S.A., and James, L.K. (2021). Single-cell analysis of human B cell maturation predicts how antibody class switching shapes selection dynamics. *Sci. Immunol.* 6, eabe6291.
- Kroeger, D.R., Milne, K., and Nelson, B.H. (2016). Tumor-infiltrating plasma cells are associated with tertiary lymphoid structures, cytolytic T-cell responses, and superior prognosis in ovarian cancer. *Clin. Cancer Res.* 22, 3005–3015.
- Kurosaki, T., Kometani, K., and Ise, W. (2015). Memory B cells. *Nat. Rev. Immunol.* 15, 149–159.
- Lindquist, R.L., Niesner, R.A., and Hauser, A.E. (2019). In the right place, at the right time: spatiotemporal conditions determining plasma cell survival and function. *Front. Immunol.* 10, 788.
- Lutz, E.R., Wu, A.A., Bigelow, E., Sharma, R., Mo, G., Soares, K., Solt, S., Dorman, A., Wamwea, A., Yager, A., et al. (2014). Immunotherapy converts nonimmunogenic pancreatic tumors into immunogenic foci of immune regulation. *Cancer Immunol. Res.* 2, 616–631.
- MacLennan, I.C. (1994). Germinal centers. *Annu. Rev. Immunol.* 12, 117–139.

- Maldonado, L., Teague, J.E., Morrow, M.P., Jotova, I., Wu, T.C., Wang, C., Desmarais, C., Boyer, J.D., Tycko, B., Robins, H.S., et al. (2014). Intramuscular therapeutic vaccination targeting HPV16 induces T cell responses that localize in mucosal lesions. *Sci. Transl. Med.* 6, 221ra13.
- Malhotra, D., Fletcher, A.L., Astarita, J., Lukacs-Kornek, V., Tayalia, P., Gonzalez, S.F., Elpek, K.G., Chang, S.K., Knoblich, K., Hemler, M.E., et al. (2012). Transcriptional profiling of stroma from inflamed and resting lymph nodes defines immunological hallmarks. *Nat. Immunol.* 13, 499–510.
- Messina, J.L., Fenstermacher, D.A., Eschrich, S., Qu, X., Berglund, A.E., Lloyd, M.C., Schell, M.J., Sondak, V.K., Weber, J.S., and Mulé, J.J. (2012). 12-Chemokine gene signature identifies lymph node-like structures in melanoma: potential for patient selection for immunotherapy? *Sci. Rep.* 2, 765.
- Meylan, M., Petitprez, F., Lacroix, L., Di Tommaso, L., Roncalli, M., Bougoüin, A., Laurent, A., Amaddeo, G., Sommacale, D., Regnault, H., et al. (2020). Early hepatic lesions display immature tertiary lymphoid structures and show elevated expression of immune inhibitory and immunosuppressive molecules. *Clin. Cancer Res.* 26, 4381–4389.
- Montfort, A., Pearce, O., Maniati, E., Vincent, B.G., Bixby, L., Böhrn, S., Dowd, T., Wilkes, E.H., Chakravarty, P., Thompson, R., et al. (2017). A strong B-cell response is part of the immune landscape in human high-grade serous ovarian metastases. *Clin. Cancer Res.* 23, 250–262.
- Nielsen, J.S., Sahota, R.A., Milne, K., Kost, S.E., Nesslinger, N.J., Watson, P.H., and Nelson, B.H. (2012). CD20+ tumor-infiltrating lymphocytes have an atypical CD27+ memory phenotype and together with CD8+ T cells promote favorable prognosis in ovarian cancer. *Clin. Cancer Res.* 18, 3281–3292.
- Nzula, S., Going, J.J., and Stott, D.I. (2003). Antigen-driven clonal proliferation, somatic hypermutation, and selection of B lymphocytes infiltrating human ductal breast carcinomas. *Cancer Res.* 63, 3275–3280.
- Perez-Shibayama, C., Gil-Cruz, C., and Ludewig, B. (2019). Fibroblastic reticular cells at the nexus of innate and adaptive immune responses. *Immunol. Rev.* 289, 31–41.
- Petitprez, F., de Reyniès, A., Keung, E.Z., Chen, T.W.-W., Sun, C.-M., Calderaro, J., Jeng, Y.-M., Hsiao, L.-P., Lacroix, L., Bougoüin, A., et al. (2020). B cells are associated with survival and immunotherapy response in sarcoma. *Nature* 577, 556–560.
- Pitzalis, C., Jones, G.W., Bombardier, M., and Jones, S.A. (2014). Ectopic lymphoid-like structures in infection, cancer and autoimmunity. *Nat. Rev. Immunol.* 14, 447–462.
- Posch, F., Silina, K., Leibl, S., Mündlein, A., Moch, H., Siebenhüner, A., Samaras, P., Riedl, J., Stotz, M., Szkandera, J., et al. (2018). Maturation of tertiary lymphoid structures and recurrence of stage II and III colorectal cancer. *Oncimmunology* 7, e1378844.
- Rodda, L.B., Bannard, O., Ludewig, B., Nagasawa, T., and Cyster, J.G. (2015). Phenotypic and morphological properties of germinal center dark zone CXCL12-expressing reticular cells. *J. Immunol.* 195, 4781–4791.
- Rodda, L.B., Lu, E., Bennett, M.L., Sokol, C.L., Wang, X., Luther, S.A., Barres, B.A., Luster, A.D., Ye, C.J., and Cyster, J.G. (2018). Single-cell RNA sequencing of lymph node stromal cells reveals niche-associated heterogeneity. *Immunity* 48, 1014–1028.e6.
- Roumenina, L.T., Daugan, M.V., Petitprez, F., Sautès-Fridman, C., and Fridman, W.H. (2019). Context-dependent roles of complement in cancer. *Nat. Rev. Cancer* 19, 698–715.
- Russick, J., Torset, C., Hemery, E., and Cremer, I. (2020). NK cells in the tumor microenvironment: prognostic and theranostic impact. Recent advances and trends. *Semin. Immunol.* 48, 101407.
- Saul, L., Ilieva, K.M., Bax, H.J., Karagiannis, P., Correa, I., Rodriguez-Hernandez, I., Josephs, D.H., Tosi, I., Egbuniwe, I.U., Lombardi, S., et al. (2016). IgG subclass switching and clonal expansion in cutaneous melanoma and normal skin. *Sci. Rep.* 6, 29736.
- Sautès-Fridman, C., Petitprez, F., Calderaro, J., and Fridman, W.H. (2019). Tertiary lymphoid structures in the era of cancer immunotherapy. *Nat. Rev. Cancer* 19, 307–325.
- Shalapour, S., Lin, X.-J., Bastian, I.N., Brain, J., Burt, A.D., Aksenov, A.A., Vrbanac, A.F., Li, W., Perkins, A., Matsutani, T., et al. (2017). Inflammation-induced IgA+ cells dismantle anti-liver cancer immunity. *Nature* 551, 340–345.
- Siliqa, K., Soltermann, A., Attar, F.M., Casanova, R., Uckley, Z.M., Thut, H., Wandres, M., Isajevs, S., Cheng, P., Curioni-Fontecedro, A., et al. (2018). Germinal centers determine the prognostic relevance of tertiary lymphoid structures and are impaired by corticosteroids in lung squamous cell carcinoma. *Cancer Res.* 78, 1308–1320.
- Silva-Cayetano, A., and Linterman, M.A. (2020). Stromal cell control of conventional and ectopic germinal centre reactions. *Curr. Opin. Immunol.* 64, 26–33.
- Tokunaga, R., Nakagawa, S., Sakamoto, Y., Nakamura, K., Naseem, M., Izumi, D., Kosumi, K., Taki, K., Higashi, T., Miyata, T., et al. (2020). 12-Chemokine signature, a predictor of tumor recurrence in colorectal cancer. *Int. J. Cancer* 147, 532–541.
- Vanhersecke, L., Brunet, M., Guégan, J., Rey, C., Bougouin, A., Cousin, S., Le Moulec, S., Besse, B., Loriot, Y., Larroquette, M., et al. (2021). Mature tertiary lymphoid structures predict immune checkpoint inhibitor efficacy in solid tumors independently of PD-L1 expression. *Nat. Cancer* 2, 794–802.
- Vano, Y., Elaidi, R.T., Bennamoun, M., Chevreau, C.M., Borchelli, D., Pannier, D., Maillet, D., Gross-Goupil, M., Tournigand, C., Laguerre, B., et al. (2020). LBA25 results from the phase II biomarker driven trial with nivolumab (N) and ipilimumab or VEGFR tyrosine kinase inhibitor (TKI) in naïve metastatic kidney cancer (m-ccRCC) patients (pts): the BIONIKK trial. *Ann. Oncol.* 31, S1157.
- Vinuesa, C.G., Linterman, M.A., Yu, D., and MacLennan, I.C.M. (2016). Follicular helper T cells. *Annu. Rev. Immunol.* 34, 335–368.
- Weiner, A.B., Vidotto, T., Liu, Y., Mendes, A.A., Salles, D.C., Faisal, F.A., Murali, S., McFarlane, M., Imada, E.L., Zhao, X., et al. (2021). Plasma cells are enriched in localized prostate cancer in Black men and are associated with improved outcomes. *Nat. Commun.* 12, 935.
- Wieland, A., Patel, M.R., Cardenas, M.A., Eberhardt, C.S., Hudson, W.H., Obeng, R.C., Griffith, C.C., Wang, X., Chen, Z.G., Kissick, H.T., et al. (2021). Defining HPV-specific B cell responses in patients with head and neck cancer. *Nature* 597, 274–278.

## STAR★METHODS

## KEY RESOURCES TABLE

REAGENT or RESOURCE	SOURCE	IDENTIFIER
<b>Antibodies for Immunohistochemistry</b>		
Rabbit polyclonal anti-CD3 concentrated at 7.5 µg/mL	Agilent	RRID : AB_2335677; Cat# : A0452
Mouse IgG2a mAb (L26) anti-CD20 concentrated at 0.6 µg/mL	Agilent	RRID : AB_2282030; Cat# : M0755
Rabbit mAb (5A1E) anti-Cleaved Caspase-3 (Asp175) diluted 1/500	Cell Signaling Technology	RRID : AB_2070042; Cat# : 9664
<b>Antibodies for Immunofluorescence</b>		
Rabbit mAb (E5I8) anti-BCL6 diluted at 1/300	Cell Signaling Technology	RRID : AB_2800138; Cat# : 89369
Rabbit anti-Carbonic Anhydrase 9/CAIX (EPR23055-5) concentrated at 0.26 µg/mL	Abcam	Cat# : ab243660
Rabbit mAb (2GV6) anti-CD3 concentrated at 0.4 µg/mL	Roche	Cat# : 790-4341
Rabbit mAb (EP204) anti-CD4 concentrated at 0.17 µg/mL	Epitomics	Cat# : AC-0173
Mouse IgG2a mAb (L26) anti-CD20 concentrated at 1.2 µg/mL	Agilent	RRID : AB_2282030; Cat# : M0755
Goat polyclonal anti-CD23 Ab concentrated at 2 µg/mL	R&D Systems	RRID : AB_354681; Cat# : AF123
Mouse IgG1 mAb (KP1) anti-CD68 concentrated at 0.2 µg/mL	Agilent	RRID : AB_2314148; Cat# : M0814
Rabbit mAb (5A1E) anti-Cleaved Caspase-3 (Asp175) diluted 1/500	Cell Signaling Technology	RRID : AB_2070042; Cat# : 9664
Rabbit mAb (EPR7785) anti-Collagen 1 concentrated at 1.8 µg/mL	Acam	RRID: AB_2861258; Cat# : ab138492
Mouse IgG1 mAb (79018) anti-CXCL12 concentrated at 10 µg/mL	Invitrogen	RRID : AB_2608710; Cat# : MA5-23547
Goat Ab anti-CXCL13 concentrated at 2 µg/mL	Invitrogen	RRID : AB_2610228; Cat# : PA5-47035
Mouse IgG2b mAb (51505) anti-CXCR5 concentrated at 5 µg/mL	R&D Systems	RRID: AB_2292654; Cat# : MAB190
Rabbit mAb (EPR5367-76) anti-IgA concentrated at 0.7 µg/mL	Abcam	RRID: AB_10976507; Cat# : ab124716
Rabbit Ab anti-IgG concentrated at 4.5 µg/mL	Agilent	RRID : AB_2335700; Cat# : A0423
Mouse IgG1 mAb (MUM1p) anti-MUM1concentrated at 4.7 µg/mL	Agilent	RRID : AB_2127157; Cat# : M7259
Mouse IgG2b mAb (195314) anti-NKp46 concentrated at 10 µg/mL	R&D Systems	RRID : AB_2149153; Cat# : MAB1850
Mouse IgG1 mAb (NAT105) anti-PD-1 concentrated 20 µg/mL	Abcam	RRID : AB_881954; Cat# : ab52587
Rat mAb (MECA-79) anti-PNAd concentrated at 50 µg/mL	BD Biosciences	RRID : AB_395099; Cat# : 553863
<b>Chemicals, peptides, and recombinant proteins</b>		
EnVision FLEX Target Retrieval Solution, High pH	Agilent	Cat# : K8004
EnVision FLEX Target Retrieval Solution, Low pH	Agilent	Cat# : K8005
H2O2 3%	Gifrer	Cat# : 10603051
Protein Block	Dako	Cat# : X0909
HighDef red IHC chromogen (AP)	Enzo	Cat# : ADI-950-140-0030
Permanent HRP Green	Zytomed	Cat# : ZUC070-100
Hematoxylin	Dako	Cat# : S3301
EcoMount	Biocare Medical	Cat# : EM897L
DAPI	Thermofisher	Cat# : 62248
ProLongTM Gold Antifade	Thermofisher	Cat# : P36934
Eosin Y alcoholic solution	Millipore Sigma	Cat# : HT110116

(Continued on next page)

**Continued**

REAGENT or RESOURCE	SOURCE	IDENTIFIER
<b>Critical commercial assays</b>		
Visium Spatial for FFPE Gene Expression Kit, Human Transcriptome	10X Genomics	Cat# : 1000336
Visium Spatial Gene Expression Starter Kit	10X Genomics	Cat# : 1000200
Dual Index Kit TT Set A	10X Genomics	Cat# : 1000215
RNeasy Kit	Qiagen	Cat# : 74004
<b>Deposited data</b>		
Frozen and FFPE spatial transcriptomics datasets	This paper	Gene Expression Omnibus (GEO): GSE175540
<b>Software and algorithms</b>		
R version 4.0.4	<a href="https://www.r-project.org/">https://www.r-project.org/</a>	<a href="https://www.r-project.org/">https://www.r-project.org/</a>
MiXCR version 3.0.13	Bolotin et al., 2015	<a href="https://github.com/milaboratory/mixcr">https://github.com/milaboratory/mixcr</a>
Space Ranger version 1.3.0	10X Genomics	<a href="https://www.10xgenomics.com/">https://www.10xgenomics.com/</a>
Halo and Halo AI	Indica Labs	<a href="https://indicalab.com">https://indicalab.com</a>
Seurat version 4.0.1	<a href="https://doi.org/10.1101/10.1016/j.cell.2021.04.048">https://doi.org/10.1101/10.1016/j.cell.2021.04.048</a>	<a href="https://satijalab.org/seurat/">https://satijalab.org/seurat/</a>
MCP-counter	Becht et al., 2016b	<a href="https://github.com/ebecht/MCPcounter">https://github.com/ebecht/MCPcounter</a>
RCTD version 1.2.0	Cable et al., 2021	<a href="https://github.com/dmcable/spacexr">https://github.com/dmcable/spacexr</a>

**RESOURCE AVAILABILITY****Lead contact**

Further information and requests for supporting data and resources should be directed to and will be fulfilled upon reasonable request by the lead contact, Wolf H. Fridman ([herve.fridman@crc.jussieu.fr](mailto:herve.fridman@crc.jussieu.fr))

**Materials availability**

Materials availability This study did not generate new unique reagents. The authors declare that all the results supporting the findings of this study are available within the paper and its figures.

**Data and code availability**

Processed spatial transcriptomic data have been deposited on the gene expression omnibus array under the accession ID GSE175540. Codes used to process data and produce figures are available at [https://github.com/maximemeylan/Meylan\\_et\\_al\\_2022](https://github.com/maximemeylan/Meylan_et_al_2022)

**EXPERIMENTAL MODEL AND SUBJECT DETAILS****Ethics and patients**

The study included primary tumors (n=130) from three cohorts of patients (Table S1). One cohort of 46 patients with more than 4 cm primary ccRCC surgically removed at the European Georges Pompidou Hospital (HEGP), included in the “Exhaustive Genetic and Immunological Characterization of Colon, Kidney and Liver Tumors” (ExhauCRF) trial registered at [ClinicalTrials.gov](https://ClinicalTrials.gov) under # NCT03149523, authorized by French Health authorities (ANSM n°2016A01458-43, CPP Ile-de-France II n°2016-07-08, IRB 00001072). A second cohort of 25 patients with primary ccRCC surgically removed by radical or partial nephrectomy at the hospital Institut Mutualiste Montsouris (Paris, France) recruited between 2015 and 2017 in the protocol “Microenvironnement des tumeurs du rein, modulation et impact clinique” approved by the medical ethics board of the participating institutions (CEPAR 2014-01). A third cohort of 59 patients with previously untreated metastatic T4 ccRCC surgically removed at HEGP, included in the french multicenter “Biomarker Driven Trial with Nivolumab and Ipilimumab or VEGFR TKI in Naïve Metastatic Kidney Cancer” (BIONIKK) trial registered at [ClinicalTrials.gov](https://ClinicalTrials.gov) under # NCT02960906 and authorized by French Health Authorities (ANSM, EUDRACT#2016-003099-28). The BIONIKK clinical trial included 199 metastatic patients treated either with Nivolumab (N), Nivolumab + Ipilimumab (NI) or Tyrosine kinase VEGFR inhibitors (TKI) (Vano et al., 2020). From the 130 primary tumors banked during the BIONIKK trial, 93 had surgical specimens from which 59 had enough material for our study, 18/59 from patients treated with Nivolumab, 35/59 with Nivolumab + Ipilimumab and 6/59 with TKI. All the included patients signed an informed consent prior to inclusion in the study. Lymphocyte and TLS were quantified on the 130 tumors from the three cohorts. TLS maturation was analyzed on the 57 TLS positive tumors. Plasma cell (PC) quantification and IgG detection was performed on 103 tumors. Artificial Intelligence (AI) based fibroblast quantification and proximity with PCs was evaluated on 44 tumors. Macrophages and NK cells were analyzed on 76 and 98 tumors respectively and

cell death quantification was performed on 85 tumors. Spatial transcriptomics was performed on 24 tumors including 12 frozen and 12 FFPE. For frozen tumors, to minimize the misassignment of tumors depending on anatomical heterogeneity, TLS presence was established both by imaging on whole tumor section and by expression of a TLS specific gene signature on frozen bulk 5' RNA sequencing which was performed on 47 samples (Figure S1; Table S1).

## METHOD DETAILS

### Sample selection for the spatial transcriptomic assay

In order to get TLS annotated samples on the frozen Visium spatial gene expression assay (10X genomics), 3 selection steps were used on tumors with both available FFPE and frozen material: 1) TLS presence was assessed by CD3/CD20 IHC on one whole FFPE tumor tissue section, 2) TLS positivity was also evaluated by expression of the 12-chemokines signature (Coppola et al., 2011) from bulk 5'RNAseq in a frozen sample from the same tumor, 3) Finally, presence of infiltrating lymphocytes was determined by MCP-counter on 5' bulk RNAseq in a frozen sample from the same tumor. Selected samples were evaluated for size, shape and overall cryo-conservation status for application on the Visium slides (10X genomics) to provide optimal coverage of the 6.5 x 6.5mm<sup>2</sup> capture areas. Selected samples were stained by toluidine to morphologically ascertain the presence of immune infiltrates and lymphocyte aggregates on the frozen material before permeabilization for the transcriptomic assay.

The selection of samples for the Visium FFPE assay was done by CD3/CD20 IHC on one whole FFPE tumor tissue section, identifying the TLS status in each FFPE tumor block. FFPE tumor blocks with relevant TLS status and DV.200 over 50 were selected for the Visium FFPE assay.

Spatial transcriptomics assayVisium spatial gene expression slides and reagents kits were used according to manufacturer instructions (10X Genomics). Each capture area (6.5 x 6.5 mm<sup>2</sup>) contains 5,000 barcoded spots that are 55 µm in diameter (100 µm center to center between spots) providing an average resolution of 1 to 10 cells and up to 100 cells inside TLS areas). Fresh frozen tumor samples were embedded in OCT, (cryo-sectioned at -10°C and processed according to the recommended protocols (Tissue optimization: CG000238 Visium 10X Genomics; Gene expression: CG000239). Optimal permeabilization time for ccRCC samples was measured at 18min. Libraries were prepared with Truseq Illumina libraries and sequenced on a NovaSeq (Illumina) at a minimum sequencing depth of 150 000 read-pairs per spatial spot by Integragen (Evry). Sequencing was performed with the recommended 10X protocol (read 1: 28 cycles; i7 index read: 10 cycles; i5 index read: 10 cycles; and read 2: 91 cycles), yielding between 200 million and 700 million sequenced reads. FFPE tumor samples were prepared according to the recommended protocols (tissue preparation guide CG000408) H&E image preparation was performed according to protocol (Deparaffinization, H&E staining, Imaging and de-crosslinking, CG000408). Due to shortage of eosin Y alcoholic solution (Millipore Sigma HT110116) for the first Visium FFPE batch, a manual preparation of alcoholic eosin solution was performed, which yielded an H&E image with lower hematoxylin staining. Tumors c\_3, c\_4, c\_10, c\_37, with low hematoxylin staining are annotated as “low hematoxylin” on **Data S1 and S2**. Spatial gene expression assay was performed according to the protocol CG000407. Libraries were prepared with Truseq Illumina libraries and sequenced on a NovaSeq (Illumina) at a minimum sequencing depth of 50 000 read pairs per spatial spot by Integragen (Evry). Sequencing was performed with the recommended protocol (read 1: 28 cycles; i7 index read: 10 cycles; i5 index read: 10 cycles; and read 2: 50 cycles), yielding between 150 million and 224 million sequenced reads.

### Bulk 5'RNA sequencing assay

Total RNA was extracted from frozen tumors using the RNeasy Kits according to the manufacturer's instructions (Qiagen). The sizing, quantitation, integrity and purity of all samples were measured using the 2100 Bioanalyzer instrument (Agilent). RNA was eluted in 50 µl RNase-free water and stored at -80°C until transcriptome profiling by RNA-Seq with the Illumina NovaSeq (IntegraGen).

### Immunohistochemistry and immunofluorescence labelling assays

7µm-thick sections from fresh frozen tumor tissue were fixed with methanol for 30 minutes at -20°C. FFPE human tumor and control specimens were cut into 3-4-µm-thick sections. Human FFPE tonsil sections and/or ccRCC test tumor sections (France Tissue Bank) were used as positive controls for BCL6, CD3, CD20, CD23, CD68, CAIX, Cleaved Caspase 3, Collagen type I, CXCL12, MUM1 (*irf4*), NKp46, PNAd, IgA and IgG. Antigen retrieval was carried out on a PT-link (Dako) using the EnVision FLEX Target Retrieval Solutions at High pH (Dako, K8004) or Low pH (Dako, K8005). Endogenous peroxidase activity and non-specific Fc receptor binding were blocked with H2O2 3% (Gifrer, 10603051) and Protein Block (Dako, X0909) respectively. The primary and secondary antibodies used for IHC and IF are summarized in key resources table. All images were independently analyzed blindly by 3 reviewers (AB, CSF, IG). Necrotic and serous areas were excluded from image analyses.

The stainings were performed manually. Chromogenic detection of TLS was performed using HighDef red IHC chromogen (AP) (Enzo, ADI-950-140-0030) for CD20, Permanent HRP Green (Zytomed Systems, ZUC070-100) for CD3 and Cleaved Caspase 3. The nuclei were counterstained with hematoxylin (Dako, S3301). After mounting with EcoMount (Biocare Medical, EM897L), the slides were scanned with a NanoZoomer (Hamamatsu).

For CD3/CD20/PD1 3-plex staining of frozen consecutive Visium slide, conventional fluorescent-dye conjugated secondary antibody system was performed manually (all secondary antibodies were diluted at 1:100). The PNAd/CD20/CD23/BCL6 4-plex staining, the CD3/CD20/PD1, PD1/CD4/CXCR5, CD20/CD3/CXCL13, IgA/IgG/MUM1, MUM1/CXCL12/Col1 and Cleaved Caspase 3/CD68/IgG 3-plex stainings, and the CAIX/IgG, CD68/Cleaved Caspase 3 and NKp46/Cleaved Caspase 3 2-plex stainings were performed

manually on FFPE tumor sections using a tyramide system amplification (TSA) and a conventional fluorescent-dye conjugated secondary antibody system (all secondary antibodies were diluted at 1:100). Nuclei were stained with DAPI Solution (Thermofisher, 62248) at 2 µg/ml for 10 minutes. After mounting with ProLong™ Gold Antifade Mountant (Thermofisher, P36934), the slides were scanned at 20X magnification using a Zeiss Axio scan Z1 device. Antibodies and TSA used are listed in key resources table.

## QUANTIFICATION AND STATISTICAL ANALYSIS

### Visium libraries pre-processing

For each frozen sample, FASTQ files and manually aligned histology images were analyzed with Space Ranger 1.1.0 which uses the STAR genome aligner version v.2.5.1b and the human reference genome hg38 (refdata-gex-GRCh38-2020). An average of 3700 median genes per spot was measured, with one batch having poorer quality metrics (tumors id: c\_2, c\_5, c\_23, c\_57) with median genes per spots ranging from 875 to 2078 median genes per spot.

For each FFPE sample, FASTQ files and manually aligned histology images were analyzed with Space Ranger 1.3.0 and the probeset provided by 10X genomics (Visium Human Transcriptome Probe Set v1.0 GRCh38-2020-A). An average of 3730 median genes per spot was measured, with median genes per spot ranging from 2385 to 5514.

### Quantitative evaluation of TLS and cell densities

TLS were identified using the registration module to fit one slide on the other (Halo10 software, Indica labs). Tumors were considered TLS-positive when a CD3 aggregate with CD20 staining was found with surface above 7,000 µm<sup>2</sup>, containing at least 100 cells, as quantified with Halo10 software (Indica labs). Density of cleaved caspase-3 positive tumor cells/mm<sup>2</sup> in tumor areas were quantified with Halo 10 software using different algorithms selecting nuclei size of tumor cells (Indicalabs).

Density of positive cells/mm<sup>2</sup>: MUM1/IgG, MUM1/IgA, CD68, NKp46 and cleaved caspase-3 in tumor area were quantified with Halo10 software (Indica labs) using the fitting counting algorithms. The percentages of membrane IgG+ and/or IgA+ tumor cells were determined from the entire tumor tissue. The averages of the percentages of membrane IgG+ and of membrane IgA+ tumor cells (as defined by nuclear size above 30 microns) were counted in the different tumoral areas using Halo 10 software. Proximity analyses between innate cells and cleaved caspase 3 positive tumor cells was performed by counting cells with a distance below 25 µm (nucleus-nucleus) in 4 randomly selected tumoral fields for 14 tumors

### Artificial intelligence (AI) assisted spatial proximity analysis

Distances between fibroblasts and PCs were computed on 44 FFPE tumor sections stained for MUM1, IgG and IgA by immunofluorescence following a three steps protocol (Figure S5). First, the pre-trained neural network Nuclei Seg (Plugin) FL v1.0.0 (Indica labs) was trained on more than 11500 nuclei from 10 different tumor sections allowing robust detection of immune, clear cell renal cell and fibroblasts (Figure S5A). Then, the Nuclei Phenotyper (Plugin) was trained from 6600 nuclei classified into 3 classes (tumor cells, immune cells or fibroblasts) from 10 tumors sections (Figure S5B). Both the nuclei segmenter and nuclei phenotyper neural networks rely on DAPI signal to detect and phenotype nuclei respectively. Finally, proximity analyses were performed with the spatial analysis module of Halo (Indica labs) by evaluating the distances between every PCs (detected by IF as MUM1<sup>+</sup> cells) located within 200 µm of a fibroblast (detected by the nuclei phenotyper neural network) (Figure S5C).

### Visium data processing

Visium pre-processed data were imported into R via Seurat V.4.0.1. Spatial spots featuring more than 30% of mitochondrial genes and less than 300 genes were filtered out, as they identified necrotic or damaged tissue areas which were validated by a pathologist (VV). Genes with counts in less than 5 spatial spots were discarded. Spots featuring folded were removed. Raw counts were normalized with the SCTransform function of Seurat using the “assay=spatial” parameter.

### Immune and stromal abundances estimation

The spatial immune and stromal infiltrates of each tumor were estimated with MCP-counter (Becht et al., 2016a) which computes abundances scores of 8 immune (T cells, CD8+ T cells, cytotoxic lymphocytes, natural killer cells, B cell lineage, monocytic lineage, myeloid dendritic cells and neutrophils), and two stromal populations (endothelial cells and fibroblasts). MCP-counter was applied on the SCT normalized scores of each tumor independently, therefore providing cell population abundance scores comparable between all spatial spots within one tumor.

### TLS annotations on the Visium data

Spatial spots belonging to TLS were defined by CD3/CD20 staining on the consecutive slide for frozen tumors or on the sample block for FFPE tumors. Selection of spatial spots belonging to TLS was performed manually using the software Loupe (10X genomics), producing TLS associated annotations which were imported into R and added to each Seurat object.

### TLS imprint signature

The TLS imprint signature was defined from 4 TLS+ tumors by differential expression analysis and AUC validation. Differential expression analysis between spatial spots annotated as TLS and the rest of the tumor using “FindMarkers” (Seurat) and MAST. Leave-one-out cross validation was performed by sequentially identifying genes from 3 tumors and validating them on the fourth one. Genes with an average fold change over 2 and adjusted p value under 0.05 were considered for the analysis. Genes reaching an AUC of 0.7 in at least 3 TLS+ tumors were selected. The signature is composed by the following genes *IGHA1*, *IGHG1*, *IGHG2*, *IGHG3*, *IGHG4*, *IGHGP*, *IGHM*, *IGKC*, *IGLC1*, *IGLC2*, *IGLC3*, *JCHAIN*, *CD52*, *CD79A*, *FCRL5*, *MZB1*, *SSR4*, *XBP1*, *TRBC2*, *IL7R*, *CXCL12*, *LUM*,

*C1QA, C7, APOE, PTLP, PTGDS, PIM2, DERL3.* The TLS imprint signature score was computed by taking the geometric mean of the 29 genes for each spot. This signature was validated on 4 frozen and 12 FFPE tumors.

#### **Single cell B cell subtypes mapping to spatial data**

Reference single-cell RNA-seq dataset from [King et al. \(2021\)](#) was downloaded from ArrayExpress (accession code E-MTAB-9005). Sample BC005 was chosen since it had the highest number of cells. Cell type annotation was also obtained from ArrayExpress. All cells were kept for the RCTD analysis pipeline ([Cable et al., 2021](#)). RCTD was run from the RCTD R package (version 1.2.0) on this reference and on Visium spatial transcriptomics data, in doublet mode set to full.

#### **Spatial co-location**

For each tumor independently we correlated expression values of gene or signature using Pearson's test. Then, for each spot, expression of the genes or signature was dichotomized by assigning "high" for spots above the median, or "low" for the spots below the median. Co-location was evidenced by global significant positive correlation coefficient and presence of "high-high" spots in relevant areas.

#### **BCR repertoire profiling**

BCR repertoire was analyzed both on 5' frozen bulk RNAseq and on 3' frozen spatial transcriptomics according to MiLaboratory quickstart recommendations. 3' frozen spatial transcriptomic libraries were deeply sequenced (150 000 reads per spots) allowing enhanced capture of mRNA transcripts of sufficient length to evaluate the full CDR3 regions of most IGL and some IGH sequences.

IGH and IGL clonotype identification and quantification was performed with MiXCR ([Bolotin et al., 2015](#)) for each bulk and spatial fastq sample. The pipeline "shotgun" was used with parameters "only-productive", "-OsaveOriginalReads=true", "contig-assembly", "impute-germline-on-export", "assemble "-ObadQualityThreshold=0". Spatial location of clonotypes was determined by reading the 10X spatial barcodes from the reads used to determine the clonotypes.

For each clonotype, V gene mutations were extracted from the "AllVAlignments" column provided by the MiXCR pipeline and summed. For bulk 5' RNAseq data, only V alignments with a "V\_qual" over 750 were considered.

V and J genes composing each clonotypes were determined from the "AllVHitsWithScore" and AllDHitsWithScore" column provided by the MiXCR analysis. Multiple V and J genes mappings were considered in the clonal assessments. Clonotypes sharing V and J genes of the same family, a CDR3 sequence of the same length and with a CDR3 Levenshtein distance inferior to 15% were considered clonal.

Distances between nucleotidic VH CDR3 sequences were computed with the Levenshtein distance using the R package Stringdist and represented with a circular tree with the package dendextend. IGH Clonotypes are represented by the leaves of the tree and identified by their translated VH CDR3 sequence and the clonal family they belong to (0: not clonal, 1 to 32 clonal) append at the end of their label. Color of the branches and labels indicate membership to a clonal family, black indicates no membership. Diameter and colors of the leaves represent the number of times each clonotype have been counted and in how many different spatial spots they have been measured in.

#### **Statistical analysis**

All analyses were performed with R (version 4.0.4) and packages Seurat (version 4.0.1). Comparisons between categorical and numerical variables were performed using Mann-Whitney tests. Correlations were computed with Pearson's correlation. A p-value threshold of 0.05 was chosen for significance. P-values have been adjusted for multiple when appropriate using the Bonferroni correction.